ACS APPLIED MATERIALS & INTERFACES

Research Article

www.acsami.org

Formation Mechanism, Degradation Behavior, and Cytocompatibility of a Nanorod-Shaped HA and Pore-Sealed MgO Bilayer Coating on Magnesium

Bo Li, Yong Han,* and Kai Qi

State Key Laboratory for Mechanical Behavior of Materials, Xi'an Jiaotong University, Xi'an 710049, China

Supporting Information

ABSTRACT: A novel bilayer coating (HT24h) was fabricated on magnesium using microarc oxidation (MAO) and hydrothermal treatment (HT). The coating comprises an outer layer of narrow interrod spaced hydroxyapatite (HA) nanorods and an inner layer of MgO containing $Mg(OH)_2$/HA-sealing-pores. The hydrothermal formation mechanism of HA nanorods on MAO-formed MgO was explored. Also, evolution of structure and bonding integrity of HT24h coating with immersion in physiological saline (PS) for 0−90 days, corrosion resistance and cytocompatibility of the coating were investigated, together with MgO containing $Mg(OH)_2$-sealing-pores (HT2h) and porous MgO (MAO) coatings. Corrosion resistance was identified by three-point bending and electrochemical tests in PS, while cytocompatibility was determined by MTT, live/dead staining, and vinculin-actin-nucleus tricolor staining assays of hFOB1.19 cells. Immersion tests indicate that cracking rather than delamination is a common feature in most areas of the coatings up to day 90 and degradation is the reason for thinning in thickness of the coatings. MAO and HT2h coatings exhibit a significant thinning due to fast degradation of MgO. However, HT24h coating shows a quite small thinning, owing to the fact that the HA nanorods underwent quite slow degradation while the underlying MgO only underwent conversion to $Mg(OH)_2$ without dissolution of the $Mg(OH)_2$. Scratch tests reveal that HT24h coating still retains relatively high bonding integrity, although the failure position changes from the MgO interior to a point between the HA and MgO layers after 90 days of immersion. HT24h coating appears far more effective than MAO and HT2h coatings in reducing degradation and maintaining the mechanical integrity of Mg, as well as enhancing the mitochondrial activity, adhesion, and proliferation of osteoblasts.

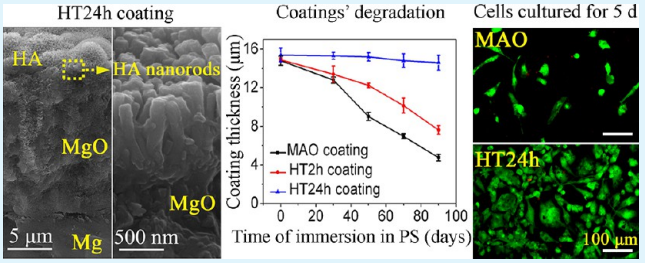

KEYWORDS: *magnesium, bilayer coating, HA nanorod, degradation behavior, mechanical integrity, cytocompatibility*

1. INTRODUCTION

Magnesium and its alloys have considerable potential in orthopedic applications, owing to their biodegradability, high strength, elastic modulus similar to that of bone, and low toxicity.[1−3] Unfortunately, the high rate of degradation and consequent loss in mechanical integrity of Mg alloys limit their clinical application.[4−7] To overcome the demerits, surface modifications of Mg alloys, such as alkaline treatment,[8,9] fluoride conversion,[6,10−12] electrodeposition,[13,14] sol−gel,[4,15−17] and microarc oxidation (MAO),[7,18−20] have been widely investigated and shown to be potential in improving corrosion resistance and mechanical integrity of the metals. Nevertheless, the improvement is not enough to allow the tissue to heal within the duration of 3−6 months.[21] For example, alkaline-treated Mg alloy was shown to undergo obvious corrosion after immersion in stimulated body fluid (SBF) for 200 h.[9] Fluoride converted Mg alloy exhibited a 40% decrease in bending strength after implantation in rabbit bone for 3 months.[6] Electrodeposited F-doped hydroxyapatite (F-HA) coatings were shown to peel off from Mg alloy after immersion in SBF for 4 weeks.[14] Sol−gel derived chitosan coatings delaminated after immersion in SBF for 10 days.[16] Moreover, the compressive strength of PCL coated Mg alloy was shown to decrease by as much as 46% after immersion in SBF for 2 months.[4] The unsatisfactory long-term protective efficacy of the coatings is attributed to the holes and cracks in the coatings,[4,9,14,16] through which corrosive medium can penetrate onto substrate, leading to pitting corrosion of Mg alloy.[22]

Alternatively, microarc oxidized (MAOed) MgO coatings can adhere firmly to Mg alloys[23] and avoid peeling off following implantation. They have been shown to provide effective protection against corrosion of Mg alloys, far exceeding the aforementioned coatings.[20] For instance, MAOed Mg alloy has been shown to retain approximately 90% of its initial strength even 12 weeks after implantation.[7] However, MAOed coatings are inherently porous, owing to the instinct spark discharging feature of MAO,[24] which seriously undermines their resistance

Received: August 13, 2014
Accepted: September 29, 2014
Published: September 29, 2014

to corrosion.[25,26] Although efforts to reduce porosity of the MAOed coatings have been done by sealing pores with SiO_2, Al_2O_3, and ZrO_2,[27,28] the sealing agents are not biodegradable and pose the risk to induce osteolysis when exposed to bone tissue.[29]

Studies on chemical composition of coatings have highlighted an enhanced role of HA in promoting adhesion, proliferation and differentiation of cells, and new bone formation compared to polymers, MgO and other inorganic components.[3,30,31] Our previous works revealed that the topography of HA on titanium also played a key role in the regulation of cell behavior. Compared to nanogranulated TiO_2, $Ca_{0.5}Sr_{0.5}TiO_3$, and Sr-HA, narrow interrod spaced Sr-HA nanorods have been shown to enhance the adhesion, proliferation, and differentiation of cells as well as the mineralization of extracellular matrix.[32−34] Hiromoto et al. hydrothermally synthesized nanorod-shaped HA coatings on Mg; however, those coatings exhibited weak adhesion to Mg, and the improvement of Mg corrosion is unexpected due to the intervals among the nanorods.[35,36] As reviewed elsewhere,[3,37] despite numerous attempts to improve the corrosion protective ability of inorganic coatings, maintaining sufficient mechanical integrity of Mg/Mg alloys for a reasonable length of time remains a challenge and the quest for the perfect strategy continues.

The degradation behavior of coatings over time is a matter of concern. It has been reported that Mg_2F coating on Mg alloy disappeared after implantation for 4 weeks,[12] and MAO coated Mg alloy was shown to disappear at week 12 of implantation.[25] In another study, electrodeposited-HA/MAOed-MgO bilayer coating could not be observed on Mg alloy after 18 weeks of implantation, in which the outer layer of HA disappeared after 12 weeks of implantation.[31] In fact, the disappearance of the coatings can be accredited to either their dissolution or disruption from substrates to generate fragments. Excessive fragmentation of coatings will incur an adverse effect on the surrounding cells.[38] Previous studies have focused mainly on the corrosion protective ability and biocompatibility of coatings on Mg alloys. The structural integrity of coatings, such as MAO coatings,[20,26,39,40] polymer coatings,[15,41,42] and conversion coatings,[12,38] during in vitro immersion or in vivo implantation has been described in outline or schematically. There remains insufficient experimental evidence to support the failure model of such coatings, and some concerns remain: (1) What is the manner to control the disappearance of coatings on Mg alloys in physiological environment, dissolution, or detachment? (2) How about the degradation rate of coatings if dissolution is a predominant manner? (3) What is the cause for the detaching of coatings?

To simultaneously endow coatings with high protective efficacy on Mg alloys, improved cell response, and therefore enhanced new bone formation, in this work, we reported our efforts to fabricate a novel bilayer coating on Mg using a two-step method of MAO and hydrothermal treatment. The resultant coating consists of HA nanorods as an outer layer as well as pores-sealed MgO with $Mg(OH)_2$ nanoplates and HA nanorods as an inner layer. The formation mechanism of HA nanorods on MgO was explored. Also, evolution of structure and bonding integrity of the HA patterned coating with immersion in physiological saline for 0−90 days, corrosion resistance, and cytocompatibility of the coating were investigated, together with the MAOed porous MgO coating and short-term HT derived $Mg(OH)_2$-sealing-pores contained MgO coating.

2. MATERIALS AND EXPERIMENTAL METHODS

2.1. Microarc Oxidation and Hydrothermal Treatment. Commercial pure Mg discs (Luoyang City Xinyou Magnesium Alloys Scientific Technology Co., Ltd., China) with a size of ϕ14 × 4 mm were used as substrates. The discs were ground successively with 100#, 400#, and 1500# abrasive papers, then ultrasonically cleaned with ethanol and distilled water prior to microarc oxidation. Subsequently, a pulse power supply (Xi'an Jiaotong University, China) was employed, and a Mg disc was used as anode while a stainless steel plate was used as cathode. The Mg discs were microarc oxidized one by one in an aqueous electrolyte containing 0.02 M β-glycerophosphate disodium ($C_3H_7Na_2O_6P{\cdot}5H_2O$, β-GP; Sinopharm Chemical Reagent Co., Ltd., China), 0.0135 M $Ca(OH)_2$ (Sinopharm Chemical Reagent Co., Ltd., China) and 0.125 M NaOH (Sinopharm Chemical Reagent Co., Ltd., China) at an applied positive pulse voltage of 450 V, a pulse frequency of 100 Hz and a duty ratio of 26% for 10 min. Such resultant coating is herein termed as MAO and the Mg discs with MAO coatings are termed as MAO coated Mg.

A Teflon-lined autoclave with a volume of 52 mL was employed for hydrothermal treatment (HT) of MAO coatings on Mg discs. 7.8 mL of aqueous solution containing 0.1 M $C_{10}H_{12}CaN_2Na_2O_8$ (Ca-EDTA) and 0.5 M NaOH was added into the autoclave, and the MAO coated Mg discs were immersed in the solution to undergo HT at 90 °C for 2, 8, and 24 h. These hydrothermally treated (HTed) MAO coatings are referred to as HT2h, HT8h, and HT24h, respectively. They are referred to overall as HT coatings.

2.2. Characterizing the Structure and Bonding Integrity of the Coatings. The chemical species of MAO coating were examined with X-ray photoelectron spectroscope (XPS; Axis Ultra, U.K.). In XPS tests, Mg Kα radiation was used as an X-ray source, and the photoelectron takeoff angle was set at 45°. The obtained XPS spectra were calibrated to C 1s (hydrocarbon C−C, C−H) contribution at the binding energy of 284.8 eV. Phase identification of MAO and HT coatings was carried out with an X-ray diffractometer (XRD; X'Pert PRO, Netherland) in $\theta-2\theta$ geometry using Cu−Kα (λ = 0.15406 nm) radiation over a 2θ angle of 20−63° at a step of 0.02°. The morphologies and elemental compositions of the coatings were examined with a field emission scanning electron microscope (FESEM; FEI QUANTA 600F) equipped with an energy-dispersive X-ray spectrometer (EDX). The nanoplate and nanorod scratched from the HT coatings were examined using transmission electron microscope (TEM; JEOL JEM-2000FX, Japan) equipped with EDX operating at 200 kV.

To identify the bonding integrity of the coatings on Mg discs, scratch tests were performed using an auto scratch coating tester, which consists of a spherical stylus (Rockwell C diamond) sliding at a constant speed across a coating surface under various loads to generate a scratch. The critical load, Lc, defined as the smallest load at which a recognizable failure occurs, was determined from the curve of acoustic output versus load, which can characterize bonding integrity of a coating. For each kind of the coatings, three samples were used and critical loads were averaged.

2.3. Immersion Tests to Evaluate Evolution of Structure and Bonding Integrity of the Coatings. The immersion tests of the MAO and HT coated Mg discs were carried out in physiological saline (PS, i.e., 0.9 wt % NaCl aqueous solution) at 37 °C together with bare Mg disc according to ASTM-G31-72.[43] Each of the samples was sealed with silastic in order to ensure exposure of only one side to the solution. After 30, 50, 70, and 90 days of immersion, the samples were removed from the solution, rinsed with distilled water and dried at air temperature. The changes in phase components as well as surface and cross-sectional morphologies of the samples after immersion in PS solution were identified using XRD and FESEM equipped with EDX, respectively. The changes in thicknesses of the coatings after immersion were identified by EDX profiles detected on their cross sections. At each immersion time point, scratch tests were carried out

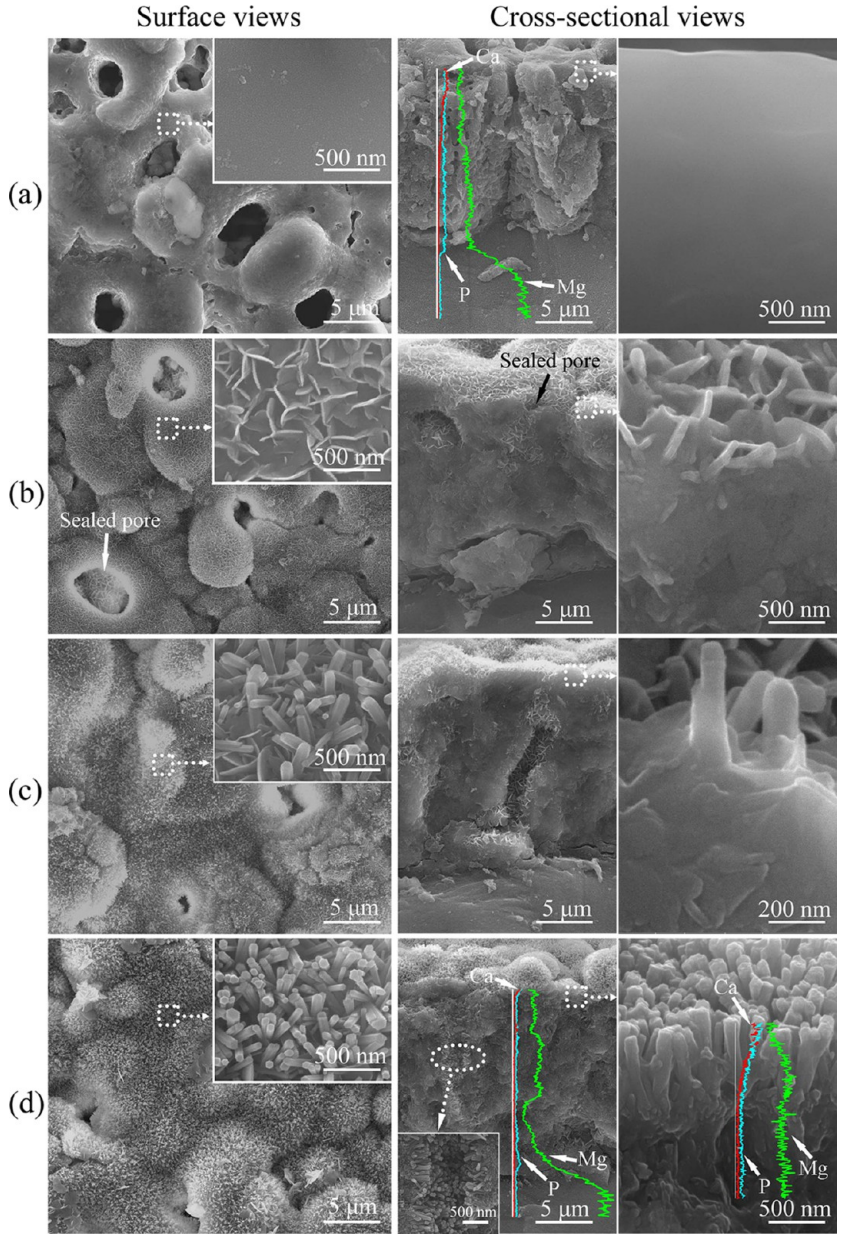

Figure 1. SEM surface and cross-sectional morphologies of MAO coating before (a) and after HT for (b) 2, (c) 8, and (d) 24 h; the insets are corresponding amplified images of the dotted-square marked areas.

to evaluate the bonding integrity of the immersed coatings on Mg discs. The hydrogen evolution and pH value of each sample immersed PS solution were also monitored. Ionic concentrations of each sample immersed solution were examined with inductively coupled plasma atomic emission spectrometry (ICP-AES; PerkinElmer, Optima 3000Dv, U.S.A.). All test values were averaged from three specimens at each immersion time point.

2.4. Evaluation of Mechanical Integrity of Bare and Coated Mg. To evaluate the mechanical integrity of bare, MAO and HT coated Mg, the ϕ3.2 × 12 mm sized cylinder-like samples, which were treated using the same processing conditions as the aforementioned MAO and HT coated Mg discs, were employed for three-point bending tests before and after immersion in PS solution at 37 °C for 30, 50, 70, and 90 days. The bending tests were performed on a mechanical test machine system (SUNS CMT 5105). Each sample was centrally positioned on two supports of the testing rig separated at a distance of 6 mm. A crosshead applied at the surface center of the sample was engaged to move downward at a rate of 0.5 mm/min, causing the sample to bend to failure at an applied load, which was defined as the maximum bending force. Each type of sample was tested in triplicate at each immersion time point and the obtained values were averaged.

2.5. Electrochemical Tests of Bare and Coated Mg. Potentiodynamic polarization tests of bare, MAO and HT coated Mg discs were performed using an Autolab potentiostat set (PGSTAT, 128 N, Metrohm) at 37 °C. Each of the samples (exposed area of 1.54 cm^2) was immersed in a three electrode cell containing PS solution under open conditions to act as a working electrode. A saturated calomel electrode (SCE) was used as the reference electrode and a graphite rod as the auxiliary electrode. After a 5 min delay under open-circuit conditions to make the samples reach a steady state, the potentiodynamic polarization curves were measured from 500 mV below the open circuit potentials (referred to the SCE) displayed on Autolab potentiostat set at a scanning rate of 5 mV/s. To investigate the corrosion resistance of the samples, electrochemical impedance spectroscopy (EIS) measurements were conducted in the experimental cell mentioned above, and carried out at the open circuit potential after immersion in the PS solution for 5 min. To ensure linearity in the

electrode response, a small amplitude sine wave (10 mV) was applied throughout the experiments at frequencies between 1×10^{-1} Hz and 1×10^{5} Hz for duration of 15 min. The impedance data were analyzed using the Zview 3.1 software (U.S.A.). To ensure the reliability of results, all potentiodynamic and EIS tests were performed in triplicate.

2.6. Cytocompatibility of Bare and Coated Mg. Human fetal osteoblast cell line, hFOB1.19, was purchased from the Institute of Biochemistry and Cell Biology of Chinese Academy of Sciences (Shanghai, China). The cells were inoculated into complete culture medium (CCM), consisting of Dulbecco's modified Eagle medium (DMEM; HyClone, U.S.A.) supplemented with 10% fetal bovine serum (FBS; HyClone, U.S.A.), 0.3 mg/mL Geneticine418 (Sigma, U.S.A.), 0.5 mM sodium pyruvate (Sigma, U.S.A.) and 1.2 g/L Na_2CO_3, and incubated in a humidified atmosphere incubator with 5% CO_2 at 37 °C. CCM was refreshed every 2 days through the incubation period.

The bare, MAO and HT coated Mg discs were sealed with silastic, thereby leaving only one side of a sample exposed to CCM. They were then placed centrally in 24-well plates with well diameters of 15 mm. hFOB1.19 cells were seeded on each sample at a density of 4×10^4 cells cm^{-2} and incubated for 1, 3, and 5 days in CCM, which was refreshed every day. MTT assays were employed to investigate the viability of cells seeded on the samples. At the end of each time period, CCM was removed from each well and the samples were washed three times with phosphate buffered saline (PBS; Sigma, U.S.A.) and then transferred to new 24-well plates. To eliminate the effects of Mg^{2+} ions on MTT solution, the cells adhered to the samples were underwent digestion using 0.5 mL 0.25% trypsin (Sigma, U.S.A.) at 37 °C for 10 min, whereupon 0.5 mL of CCM was added to halt digestion and consequently, cell suspensions were obtained. The cell suspensions were quickly centrifuged and resuspended in 250 μL fresh CCM, and then, the cells were reseeded in new 48-well plates and incubated for 24 h to allow the cells to fully attach in order to facilitate MTT assays. Following removal of CCM from each well and subsequent washing with PBS (three times), 15 μL of MTT (Sigma, U.S.A.) solution (5 mg/mL MTT in PBS) was added with 250 μL of CCM and cultured for 4 h. The medium was subsequently removed and 100 μL of dimethyl sulfoxide (DMSO; Sigma, U.S.A.) was added to each well and oscillated for 10 min. The resulting DMSO solution was transferred to new 96-well plates and the absorbance was measured at 490 nm. Four specimens from each group were tested, and each test was repeated four times ($n = 4$).

Live/dead staining using the LIVE/DEAD Viability/Cytotoxicity Kit (Molecular Probes, Invitrogen, France) was performed to identify viable and nonviable hFob 1.19 cells on bare and coated Mg after 1, 3, and 5 days of incubation. At the end of each time period, the cell-adhered samples were washed three times using PBS followed by the addition of 500 μL of PBS containing ethidium-homodimer-1 (4 μM) and calcein-AM (2 μM) to each well prior to incubation at 37 °C for 30 min. The fluorescence-stained cells were analyzed using an OLYMPUS laser confocal microscope (FV1000) for the collection of images of four random fields on each sample. We then used these images to quantify the average number of adhered live cells (stained green with calcein AM).

Fluorescence staining of actin, vinculin and cell nucleus was performed with a triple staining kit (Chemicon International, U.S.A.) as follows. After 24 h of culture, the cells seeded samples were fixed using 4% paraformaldehyde, permeabilized using 0.1% Triton X-100 (Sigma, U.S.A.), and washed three times using PBS buffer (PBS supplemented with 0.05% Tween-20; Sigma, U.S.A.). The cells were then incubated in a 1% bovine serum albumin (Sigma, U.S.A.) blocking agent at 37 °C for 30 min. Mouse monoclonal antivinculin (2 μg/mL) was added to the cells and the cells were incubated at 37 °C for 60 min. Fluorescein isothiocyanate conjugated goat antimouse IgG (10 μg/mL; Chemicon International, U.S.A.) and 37.5 ng/mL tetramethyl rhodamine isothiocyanate conjugated phalloidin were added to the cells and the cells were incubated at 37 °C for 60 min for staining of vinculin and actin, respectively. The cells were subsequently incubated in 0.1 μg/mL 6-diamidino-2-phenylindole at 37 °C for 5 min for staining of cell nucleus. Following each of the staining procedures, the samples were washed three times using PBS buffer, whereupon the cells were examined using an OLYMPUS laser confocal microscope (FV1000).

The data were analyzed using SPSS 14.0 software (SPSS, U.S.A.). Two-way ANOVA and the Student–Newman–Keuls post hoc test were used to determine the level of significance. $p < 0.05$ was considered to be significant, and $p < 0.01$ and $p < 0.001$ were considered to be highly significant.

3. RESULTS AND DISCUSSION

3.1. Formation and Structure of MAO and HT Coatings. The phase components of MAO coating before and after HT for 2, 8, and 24 h in aqueous solution containing Ca-EDTA and NaOH are shown in Figure S1a (Supporting Information). It is revealed that MAO coating comprises single phase of MgO, HT2h coating consists of MgO and $Mg(OH)_2$; HT8h and HT24h coatings are composed of MgO, $Mg(OH)_2$, and HA, in which more HA appears on HT24h than HT8h. XPS analysis indicates that besides the predominant elements of Mg and O, MAO coating also contains Ca and P, which are in the form of Ca^{2+} and PO_4^{3-} (Figure S1b–d, Supporting Information).

Figure 1 shows surface and cross-sectional morphologies of the coatings. MAO coating is microporous with pores of 2–3 μm in diameter distributed homogeneously over its surface (left image in Figure 1a). It is uniform in thickness with a value of about 15 μm, as identified by EDX cross-sectional profiles of Mg, Ca, and P; a number of microarc discharge generated pores distribute across the entire coating (right image in Figure 1a). However, the coating matrix in both surface and cross-sectional views presents a smooth and quite dense structure, consisting of MgO as confirmed by Figure S1a (Supporting Information), without discontinuity at the interface between the coating and Mg substrate. After HT for 2 h, the surface and pores' walls of the resulting HT2h coating were covered with plate-like crystals (about 45 nm in plate thickness) composed of $Mg(OH)_2$ as confirmed by TEM (Figure S2a, Supporting Information); meanwhile, the nanoplates filled in the pores to partially seal them (as marked by arrows in Figure 1b). At 8 h of HT, short nanorods with a mean diameter of 91 ± 9.1 nm sparsely appeared on the surface of the resulting HT8h coating, among which $Mg(OH)_2$ nanoplates can be clearly observed (left image in Figure 1c). Clearly, the nanorods directly nucleated and grew on compact MgO matrix rather than on $Mg(OH)_2$ nanoplates (right image in Figure 1c). With prolonging the HT time to 24 h (e.g., for HT24h coating), these nanorods underwent significant growth in length but almost no coarsening in diameter and became compact with interrod spacing of about 63.9 ± 9.0 nm (Figure 1d). They fully covered the coating surface and grew on the walls of pores to further seal them (as revealed by the inserted amplified view of the circle-marked region in right image of Figure 1d). The nanorods consist of well-crystallized HA single crystal, growing along the *c*-axis of the hexagonal crystal, as identified by TEM (Figure S2b, Supporting Information) and described in details in Supporting Information. With the aid of EDX profiles of Ca, P, and Mg on the cross-section of HT24h coating, it is clear that the coating is two-layered with HA nanorods interspersed with $Mg(OH)_2$ nanoplates as an outer layer and MgO as an inner layer adjacent to Mg substrate.

The formation of $Mg(OH)_2$ nanoplates and subsequent HA nanorods during the HT of the MAOed P- and Ca-containing MgO layer in an aqueous solution containing Ca-EDTA and

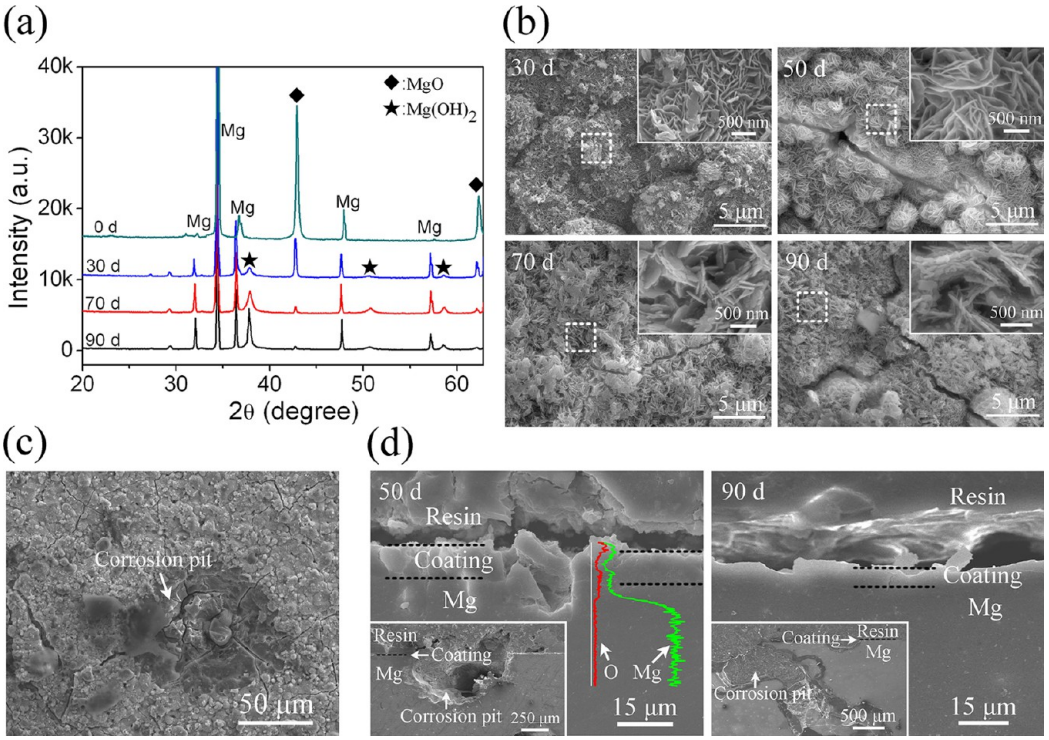

Figure 2. (a) XRD patterns, (b) surface and (d) cross-sectional SEM morphologies of MAO coating immersed in PS solution for 0−90 days (as marked in the pictures); the insets in (b) are corresponding amplified images of the dotted-square marked areas. (c) Low magnification surface view of the 90 days immersed MAO coating.

NaOH can be described as follows: first, the hydroxyl groups and water molecules in the hydrothermal solution attacked the outermost layer of the MgO to generate $Mg(OH)_2$ nanoplates according to the following equation: $MgO + H_2O \rightarrow Mg(OH)_2$. In parallel to the formation of $Mg(OH)_2$, the migration of the PO_4^{3-} and Ca^{2+} incorporated in the MgO layer occurred, having a tendency from the interior of MgO to its surface, as shown in Figures S3a and S3b (Supporting Information). Our previous works have revealed that Ca^{2+} and PO_4^{3-} incorporated in TiO_2 layer can migrate out from the interior of TiO_2 to its surface during HT.[23,32] Once the local Ca^{2+} and PO_4^{3-} in the outermost layer of the MgO reached critical concentrations due to migration, becoming supersaturated with respect to HA, they reacted with hydroxyl groups in the hydrothermal solution to form HA nuclei on MgO (as confirmed by the amplified view of right image in Figure 1c). Noticeably, in the above-mentioned processing of HA nanorods, P required for HA formation only comes from the PO_4^{3-} incorporated in the MgO layer, while Ca required for HA formation may be supplied neither by the Ca^{2+} incorporated in the MgO layer or by HT solution containing Ca-EDTA. To identify the role of the Ca^{2+} incorporated in the MgO layer with regard to the formation of HA, we hydrothermally treated the aforementioned Ca and P containing MgO layer in an aqueous solution containing NaOH without Ca-EDTA for 24 h. This resulted in a few of short HA nanorods to sparsely appear on the MgO layer (Figure S4, Supporting Information). We also performed hydrothermal treatment of a MgO layer with P but without Ca in an aqueous solution containing NaOH and Ca-EDTA. This resulted in the formation of almost no HA nanorods up to 8 h; however, very long HA nanorods sparsely appeared among rather than on $Mg(OH)_2$ nanoplates at 24 h of HT (Figure S5, Supporting Information). These results indicate that during the HT of the Ca- and P-containing MgO layer in aqueous solution containing Ca-EDTA and NaOH, Ca^{2+} ions that migrated out from the interior of MgO layer played a crucial role in the nucleation of HA on MgO. In contrast, Ca^{2+} ions supplied by thermal dissociation of Ca-EDTA in the HT solution partially participated in the nucleation of HA and played a predominant role in the growth of HA nanorods. The HA nuclei increased and grew in length at the expense of PO_4^{3-} migrating out from MgO and Ca^{2+} mainly dissociated from Ca-EDTA. The process of HA formation and morphology evolution is schematically shown in Figure S3c (Supporting Information), in which the roots of HA nanorods are embedded in the MgO matrix and the existing $Mg(OH)_2$ nanoplates are interspersed within the HA nanorods, as supported by Figure 1c.

3.2. Structural Evolution of the Coatings in PS Solution. The above-mentioned highlights that MAO coating is composed of porous MgO, HT2h coating consists of MgO containing pores sealed with $Mg(OH)_2$ nanoplates as an inner layer and a thin coverage of $Mg(OH)_2$ nanoplates as an outer layer. Moreover, HT24h coating comprises an inner layer of MgO containing pores sealed with HA nanorods and $Mg(OH)_2$ nanoplates as well as an outer layer of narrow interrod spaced HA nanorods, in which the roots of the HA nanorods are embedded in the MgO matrix and the $Mg(OH)_2$ nanoplates are among the HA nanorods. These coatings, to different extent, underwent structural evolution in PS solution.

The XRD patterns as well as surface and cross-sectional morphologies of MAO coating immersed in PS for 0−90 days are shown in Figure 2. It is clear that the intensities of MgO peaks become weak while $Mg(OH)_2$ peaks appear and turn to enhance with immersion (Figure 2a), indicating the occurrence of conversion of MgO to $Mg(OH)_2$. Correspondingly, its surface morphology of pores' walls changes from compact

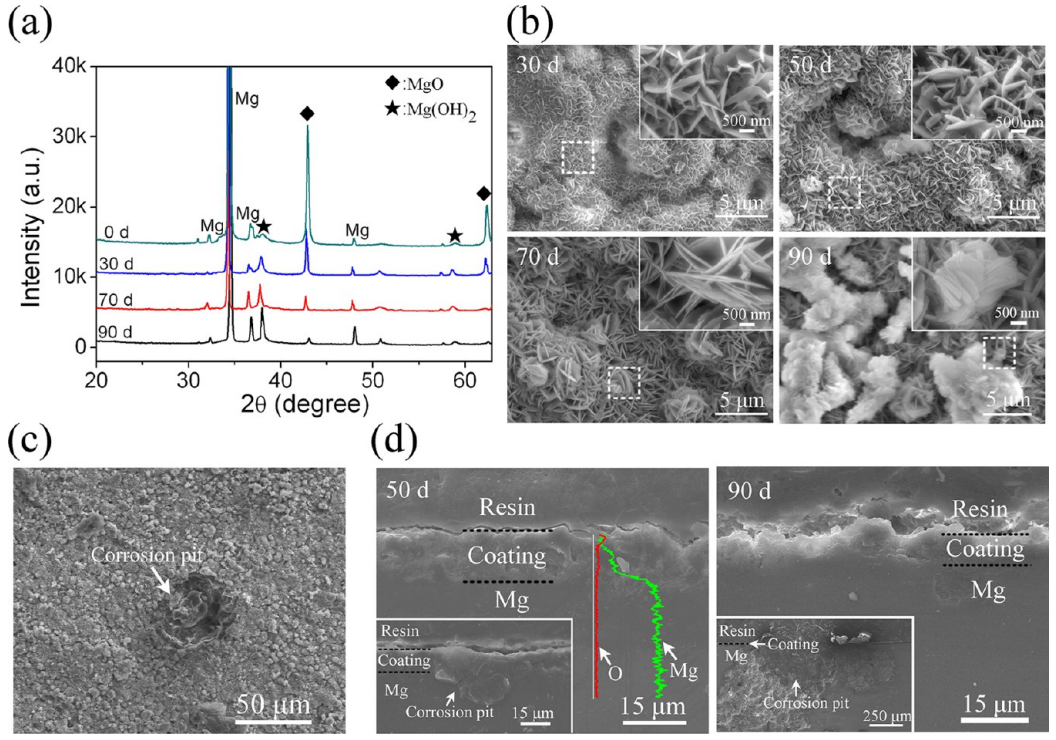

Figure 3. (a) XRD patterns, (b) surface and (d) cross-sectional SEM morphologies of HT2h coating immersed in PS solution for 0−90 days (as marked in the pictures); the insets in part b are corresponding amplified images of the dotted-square marked areas. (c) Low magnification surface view of the 90 days immersed HT2h coating.

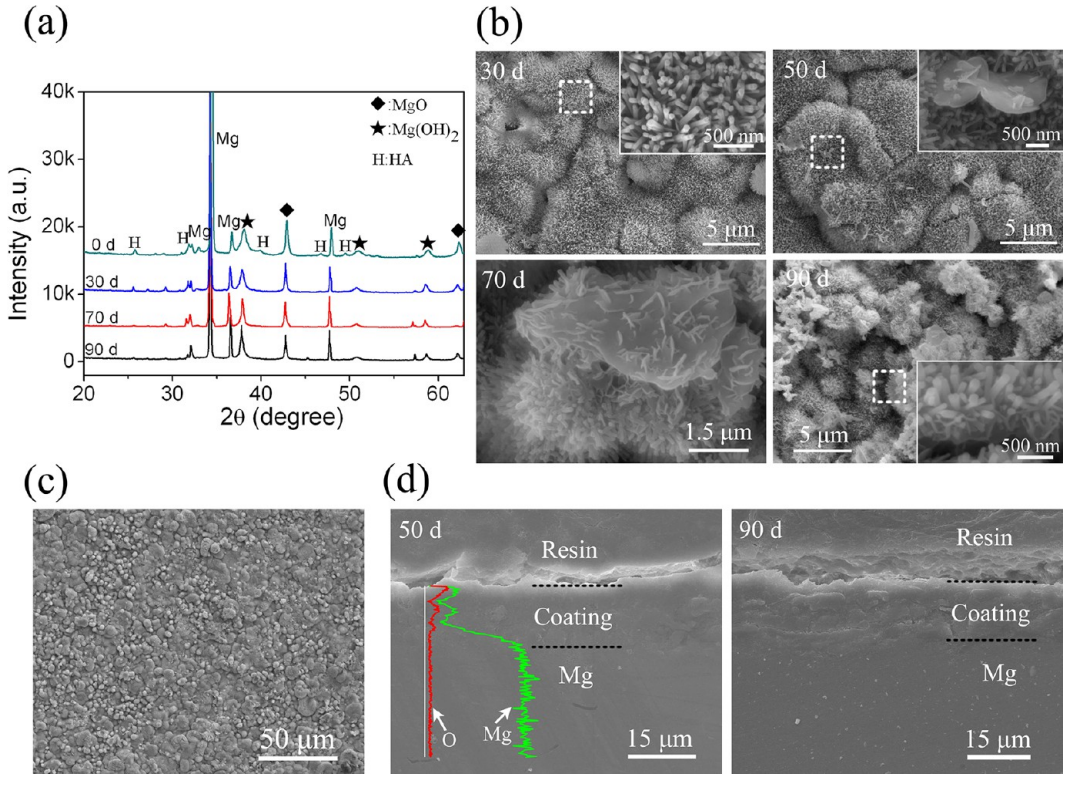

Figure 4. (a) XRD patterns, (b) surface and (d) cross-sectional SEM morphologies of HT24h coating immersed in PS solution for 0−90 days (as marked in the pictures); the insets in part b are corresponding amplified images of the dotted-square marked areas. (c) Low magnification surface view of the 90 days immersed HT24h coating.

pattern to nanoplate-like pattern after 30 days of immersion (Figure 2b), suggesting that the nanoplates consist of $Mg(OH)_2$. The $Mg(OH)_2$ nanoplates become larger on days 50 and 70 and accumulate together on day 90. As confirmed by Figure S6 (Supporting Information), the nanoplate-like $Mg(OH)_2$ layer is about 200 nm in thickness on day 30 and tends

dx.doi.org/10.1021/am505437e | ACS Appl. Mater. Interfaces 2014, 6, 18258−18274

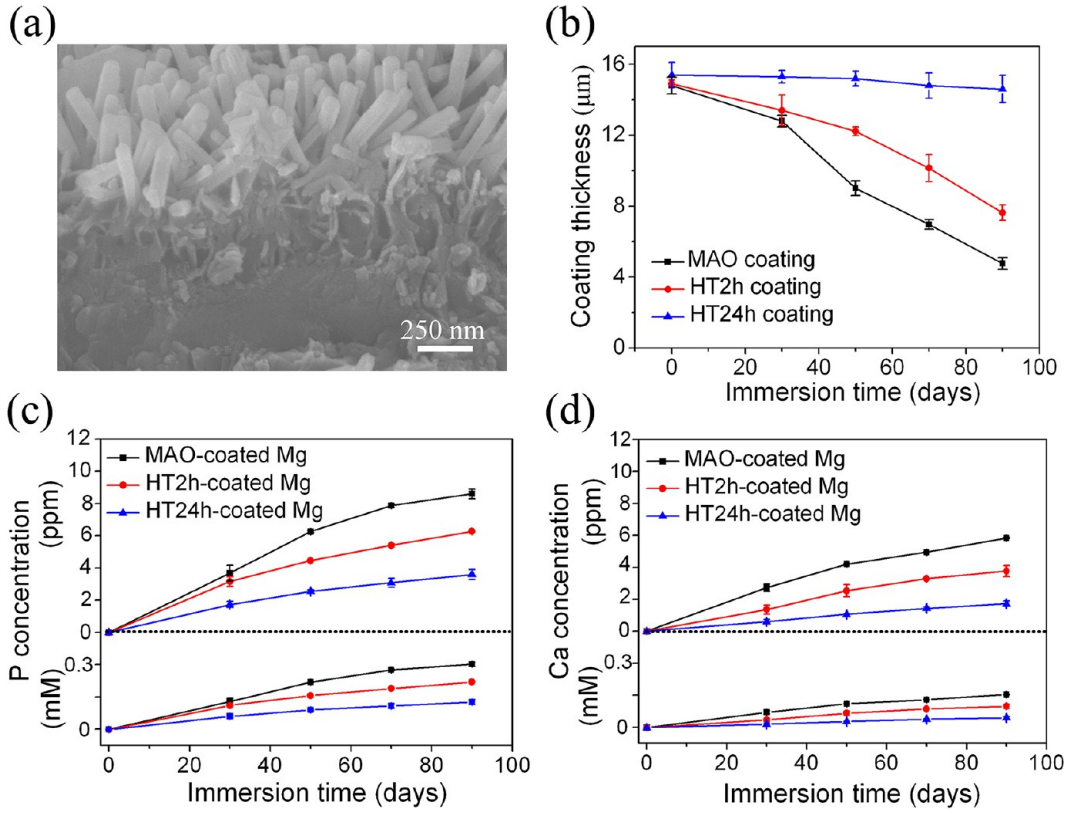

Figure 5. (a) Amplified cross-sectional view taken at the upper region of HT24h coating immersed in PS solution for 90 days. Changes in (b) thicknesses of MAO, HT2h, and HT24h coatings, (c) P and (d) Ca concentrations (shown in two kinds of units, ppm and mM) of the PS solutions immersing the coatings coated Mg as a function of immersion time.

to thicken with immersion up to 70 days, after which no significant difference in thickness can be observed, having a value of about 550 nm. At each immersion time point, there is no discontinuity at the interface of $Mg(OH)_2$ and MgO layers. Simultaneously, cracks appear on the coating surface and become more and wide with immersion (Figure 2b). It is worth noticing that after immersion for 90 days, the coating also reveals corrosion pits in some areas besides cracking as a common feature (Figure 2c). Figure 2d shows that the coating turns to thinning significantly in thickness with immersion, which is identified by EDX profiles of Mg and O (an example is shown on the 50 days immersed one). In addition, pitting corrosion of Mg substrate occurred at some places beneath the coating due to the penetration of corrosive fluid through pores in the coating onto the substrate and was aggravated with immersion, as proved by the insets (days 50 and 90) in Figure 2d.

Moving to HT2h coating, Figure 3 displays its structural evolution in PS solution for 0−90 days. XRD patterns (Figure 3a) reveal the conversion of MgO to $Mg(OH)_2$ in HT2h coating; however, the conversion is less pronounced in this coating compared to MAO coating, as identified by the corresponding intensities of MgO peaks in Figures 3a and 2a. The surface views in Figure 3b show that the $Mg(OH)_2$ nanoplates on HT2h coating are larger on day 30 compared to the unimmersed one (Figure 1b). In addition, at each immersion time point, they are larger than those on MAO coating. Simultaneously, white aggregates appear on the $Mg(OH)_2$ nanoplates and become more numerous and larger with immersion. These aggregates are, in fact, composed of fine $Mg(OH)_2$ nanoplates, as identified by the inset (day 90) in Figure 3b. A comparison of Figures 3c and 2c shows that cracking also occurred on HT2h coating with immersion; however, there are fewer of these cracks and corrosion pits and most of them are smaller than those on MAO coating at the same immersion time. The cross-sectional views depicted in Figure 3d indicate that the thinning of HT2h coating and pitting corrosion of Mg substrate did occur; however, the effects are less pronounced than those on MAO coating at the same immersion time.

Focusing on HT24h coating, its structural evolution in PS solution for 0−90 days is shown in Figure 4. Based on the evidence that the intensities of MgO peaks just slightly decrease while those of $Mg(OH)_2$ peaks slightly increase with immersion (Figure 4a), it is suggested that the conversion of MgO to $Mg(OH)_2$ was greatly inhibited in HT24h coating compared to MAO and HT2h coatings. As revealed by Figure 4b, the surface of HT24h coating displays no visible difference in morphology before (Figure 1d) and after immersion for 30 days. On day 50, larger nanoplates appear among the HA nanorods and some of them are observed to fuse together; they further fuse into much larger aggregates above the HA nanorods, as presented by the picture taken on day 70. The aggregates become more in amount with prolonging immersion time to 90 days and cracks are pronounced on the HA nanorods patterned layer at this immersion time. It can be observed from the cracking gap (the inserted picture taken on day 90) that the HA nanorods sustained MgO has converted to nanoplate-like $Mg(OH)_2$, which is responsible for cracking. However, the number of cracks is less pronounced on HT24h coating compared to MAO and HT2h coatings following immersion for the same duration, as illustrated in a comparison of Figure 4c with

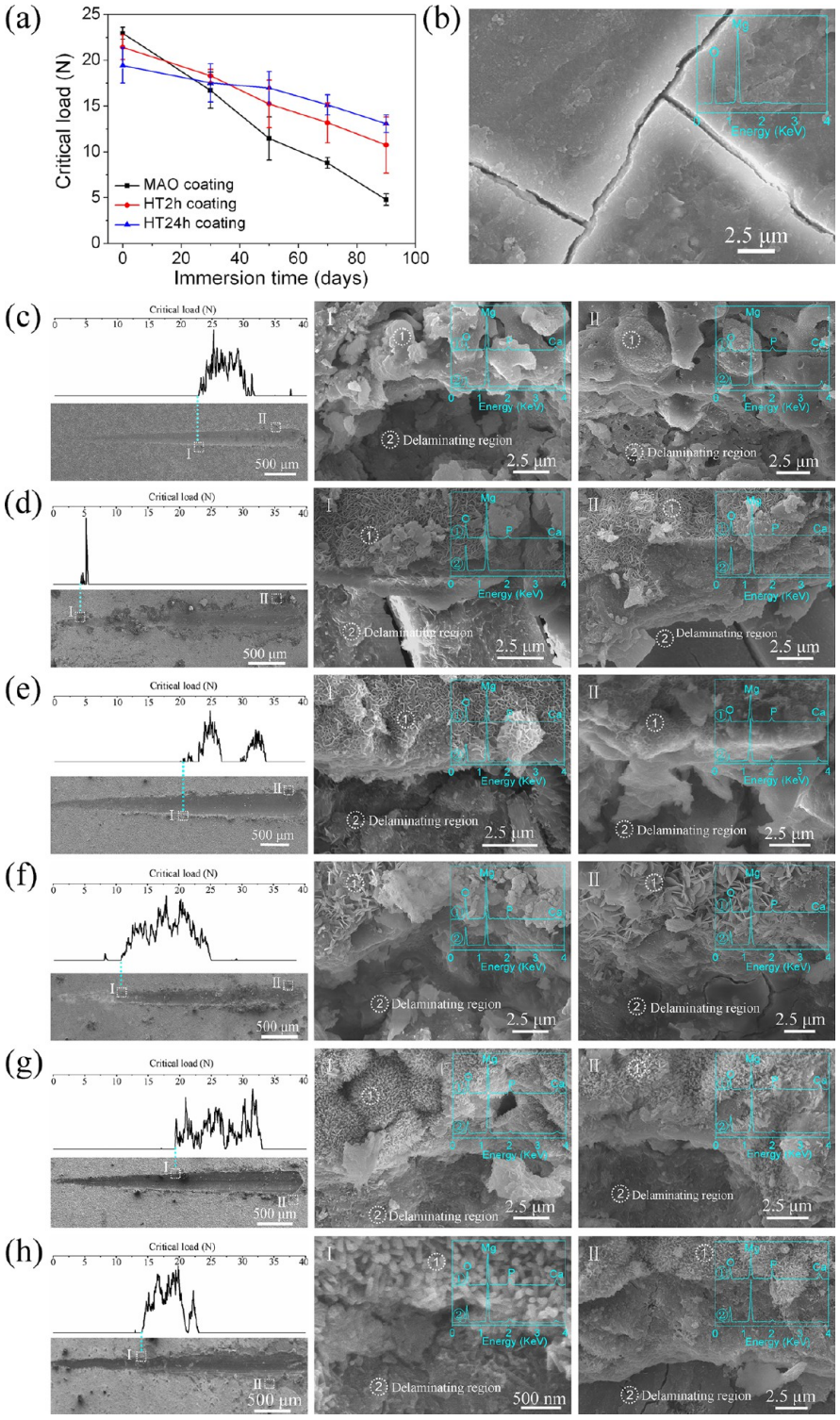

Figure 6. (a) Changes in scratch-measured critical loads of MAO, HT2h, and HT24h coatings with time of immersion in PS solution. (b) Surface morphology of bare Mg immersed in PS solution for 30 days together with the inserted EDX spectrum detected on the surface. Curves of acoustic output versus load and scratch morphologies of MAO coating without (c) and with (d) immersion for 90 days, HT2h coating without (e) and with (f) immersion for 90 days, and HT24h coating without (g) and with (h) immersion for 90 days, together with the amplified views of the areas of I-marked initial failure caused by Lc and II-marked end failure caused by load far greater than Lc; the inserted EDX spectra in each of the amplified views were detected on the 1-marked surface and 2-marked delaminating region of corresponding coating, respectively.

Figures 2c and 3c. The cross-sectional views in Figure 4d indicate that HT24h coating does not present obvious change in thickness with immersion up to 90 days. In addition, the pitting corrosion of Mg at the MgO/Mg interface in HT24h coated system is less pronounced than in MAO and HT2h coated systems after immersion for the same duration.

Figure 5a shows an amplified cross-sectional image taken at the upper uncracking region of HT24h coating immersed for 90 days. After 90 days of immersion, the HA nanorods exhibit

dx.doi.org/10.1021/am505437e | ACS Appl. Mater. Interfaces 2014, 6, 18258−18274

little change in diameter (initial 92.8 ± 9 nm versus 86.9 ± 10.6 nm), and a decrease in length from initial 602.3 ± 43.4 nm to 425.3 ± 34.8 nm, indicating that the degradation rate of hexagonal HA nanorod varies according to the crystal planes: approximately 2 nm/day for prism-facet (e.g., $(01\bar{1}0)$ plane) and almost 0 nm/day for basal-facet (e.g., (0001) plane). As known, the (0001) plane of HA is more stable than the $(01\bar{1}0)$ plane in an aqueous environment.[44,45] The crystal planes parallel to (0001) plane of F-HA has been experimentally proved to undergo the least degradation, while those perpendicular to (0001) plane degrade more quickly.[14] In the region shown in Figure 5a, the HA nanorods underlying nanoplate-like $Mg(OH)_2$ layer is about 298 nm in thickness, lower than that on MAO coating at day 90. This $Mg(OH)_2$ layer is MgO-converted during immersion rather than HT formed one, because the HTed $Mg(OH)_2$ nanoplates are located among the HA nanorods. Moreover, no gap can be observed between the HA and $Mg(OH)_2$ layers or between the $Mg(OH)_2$ and MgO layers, indicating that the HA underlying MgO in HT24h coating only underwent conversion to $Mg(OH)_2$ without dissolution of the converted $Mg(OH)_2$ during the immersion period of 90 days. The reason for this remains unclear; however, it may be partially related to the coverage of HA.

Overall, the MAO, HT2h, and HT24h coatings underwent, at different levels, a series of structural changes during immersion, including conversion of MgO to $Mg(OH)_2$, cracking, and thinning in thickness. Based on the evidence that cracking rather than delamination is a common feature in most areas of the coatings (Figures 2c–4c), the changes in the thickness of the coatings with immersion (as summarized in Figure 5b) appear to result from the degradation of the coatings. In this figure, the thicknesses were determined with the aid of Mg and O profiles detected by EDX on the cross sections, as shown in Figure S7 (Supporting Information). The average degradation rates of MAO, HT2h, and HT24h coatings are about 110, 80, and 8 nm/day, respectively. Figure 5(c and d) shows the changes in P and Ca concentrations of the PS solutions following immersion of the coated Mg. The detected P and Ca in the MAO and HT2h coated Mg immersed solutions are mostly attributed to the degradation of MgO in both of the coatings. In the case of immersing HT24h coated Mg, the detected P concentration is higher than that of Ca at each immersion time point; owing to more release of Ca than P ions resulting from the degradation of HA as well as higher content of P than Ca in the HA underlying MgO layer (as displayed by EDX profiles in Figure 1d), it is suggested that the migration of P and Ca from the MgO and its upper converted $Mg(OH)_2$ layers into the solution occurred during immersion. Thus, the detected P and Ca in the solution following immersion of HT24h coating are attributed not only to the degradation of HA but also to the migration of P and Ca from the MgO and converted $Mg(OH)_2$ layers. The result of P and Ca release further proves that the degradation of MAO coating is more pronounced than that of HT2h coating and much more pronounced than that of the HT24h coating. This is evidenced by the fact that the increments in P and Ca concentrations of the PS solutions immersing the samples at one time point relative to the former follow the following trend: MAO > HT2h > HT24h. It has previously been demonstrated that the degradation of MgO in Cl^--containing solution is caused by two reactions: $MgO + H_2O \rightarrow Mg(OH)_2$, $Mg(OH)_2 + Cl^- \rightarrow MgCl_2 + OH^-$.[21] Our result in Figure S6 (Supporting Information) clearly illustrates that the dissolution rate of $Mg(OH)_2$ is lower than the conversion rate of MgO, suggesting that the conversion of MgO is the predominant process associated with the degradation of MgO. Meanwhile, HA nanorods are degradable but undergo quite slow degradation in length and little degradation in diameter (Figure 5a). Based on the above-mentioned reasons, it is easier to understand why the sealing of pores in the MAOed MgO with HA and $Mg(OH)_2$ can greatly inhibit the degradation of HT24h coating compared with MAO and HT2h coatings.

3.3. Evolution of Bonding Integrity of the Coatings Immersed in PS Solution. In scratch test, critical load (Lc) can characterize the bonding integrity of a coating, for example, either the adhesive strength between the coating and substrate or the cohesive strength of the coating, depending on failure occurring at the coating/substrate interface or in the interior of the coating under this load. Figure 6a shows the critical loads of MAO and HT coatings, which are 22.9 ± 0.6 N for MAO coating, 21.4 ± 1.3 N for HT2h coating, and 19.4 ± 1.9 N for HT24h coating, respectively. Figures 6c, e, and g depict acoustic output versus load curves and the scratch morphologies of the coatings, including amplified views of the I-marked area of initial failure caused by Lc and the II-marked area of end failure caused by load far exceeding Lc. It is revealed that delaminations in the I- and II-marked areas occurred in the interiors of MgO layers within the coatings, as proved by the inserted EDX spectra. This result indicates that the critical loads characterize the cohesive strengths of the coatings and that the adhesive strengths between the coatings and substrates are higher than the Lc values. Noticeably, hydrothermal treatment resulted in a slight decrease in cohesive strength of the MgO layer, due to the migration of PO_4^{3-} and Ca^{2+} ions out of the MgO during HT, as evidenced by Figure S3 (Supporting Information). Despite the fact that Hiromoto and coauthors hydrothermally synthesized nanorod-shaped HA on Mg, a $Mg(OH)_2$ layer was formed between the HA layer and Mg, which enabled the HA to easily peel off the substrate.[35,36] In contrast, the HA nanorods in our HT24h coating are embedded in MgO matrix and the existed $Mg(OH)_2$ nanoplates are among the HA nanorods, this construction endows the coating with higher adhesive and cohesive strength.

Figure 6a also shows that the Lc values of the three kinds of coatings tend to decrease with prolonging time of immersion in PS solution. However, the decrease in Lc of MAO coating is greater than that of HT2h coating, and far greater than that of HT24h coating. After 90 days of immersion, the Lc values are 4.8 ± 0.6 N for MAO coating, 10.7 ± 3.1 N for HT2h coating and 13.1 ± 1.0 N for HT24h coating, respectively. The 90 days immersed MAO coating is observed that the delaminations in the areas of I-marked initial failure and II-marked end failure occurred at the MgO/Mg interface (Figure 6d). This is supported by the fact the characteristic element P, which is distributed throughout the entire MgO layer (Figure 1a), cannot be detected by EDX in the delaminating regions (Figure 6d). The appearance of O in these regions is most probably attributed to the Mg degradation derived $Mg(OH)_2$, as indicated by Figure 6b. This, in turn, suggests that the Mg adjacent to the MgO/Mg interface was corroded to $Mg(OH)_2$ after 90 days of immersion, thereby weakening the adhesive strength between the coating and substrate. For the 90 days immersed HT2h coating (Figure 6f), the delamination in the area of I-marked initial failure is observed to occur at the upper $Mg(OH)_2$/MgO interface, while the delamination in the area of

II-marked end failure is observed to occur at the MgO/Mg interface with the aid of Figure 6b. Regarding to the 90 days immersed HT24h coating, the delamination in the area of I-marked initial failure is observed to occur between the HA and MgO layers, while the delamination in the area of II-marked end failure is observed to occur in the interior of MgO adjacent to the MgO/Mg interface. This is supported by the fact the MgO-traced element P still can be detected by EDX in the delaminating region, in which the intensity of P peak is far weaker than that detected on the coating surface (Figure 6h). This result, on the other hand, indicates that even after 90 days of immersion, most of the Mg adjacent to the MgO/Mg interface did not suffer from corrosion to convert to $Mg(OH)_2$, and thereby, the MgO/Mg interface maintained strong bonding characteristics.

It is known that when Mg contacts with an aqueous solution, the following reactions occur: $Mg + H_2O \rightarrow H_2 + OH^- + Mg^{2+}$, $OH^- + Mg^{2+} \rightarrow Mg(OH)_2$,[1] resulting in Mg degradation, H_2 evolution, $Mg(OH)_2$ formation, and alkalization (an increase in pH) of the solution. Therefore, the progress of Mg degradation and thus its derived $Mg(OH)_2$ formation can be monitored by hydrogen evolution, as shown in Figure 7a. It is indicated that the degradation of Mg adjacent to the MgO/Mg interfaces in the MAO and HT coated Mg and its derived $Mg(OH)_2$ tend to increase with immersion. Following immersion for the same duration, the Mg degradation derived $Mg(OH)_2$ is less in amount for HT24h coated Mg than HT2h coated Mg and far less than MAO coated Mg. These findings are consistent with the morphological observations displayed in Figures 2d–4d and 6d, f, and h. Compared with HT2h and HT24h coatings, the greater number of pores in MAO coating enable corrosive fluid to penetrate into the coating and onto the substrate easily, leading to more $Mg(OH)_2$ to form within the pores and at the MgO/Mg interface. The formation of $Mg(OH)_2$ could exert stresses due to larger molar volume of $Mg(OH)_2$ compared with MgO,[39,46] resulting in more cracks to develop within MgO and at MgO/Mg interface in MAO coating compared to HT2h and HT24h coatings. Furthermore, the attacking of the $Mg(OH)_2$ at the MgO/Mg interface by Cl^- in the PS can aggravate cracking, further weakening the adhesion of MAO coating to Mg. It is the increase in amounts of $Mg(OH)_2$ and cracks that causes the decrease in the critical loads of the coatings with immersion. Also, the difference in increments of $Mg(OH)_2$ and cracks among the 90 days immersed coatings makes their delaminating positions different under the corresponding critical loads.

Besides the aforementioned changes in structure and bonding integrity of the coatings, the degradation of the coatings and underlying Mg can also alter the pH values and Mg^{2+} concentrations of their surrounding PS solutions, as shown in Figure 7b and c. The pH values and Mg^{2+} concentrations of the bare and coated Mg immersed solutions tend to increase with immersion time. At each immersion time point, the alkalization and Mg^{2+} concentrations of the coated Mg immersed solutions are lowered compared to the bare Mg immersed solution, especially for the HT24h coated Mg immersed solution. During the initial immersion period of 5 days, the pH values of the solutions immersing HT24h, HT2h, and MAO coated Mg are less than 9.05, 9.25, and 9.57, respectively (the inset in Figure 7b), while that of the bare Mg immersed solution reaches 10.17 on day 1. This phenomenon is ascribed to the inhibition of Mg and MgO degradation by HA nanorods and $Mg(OH)_2$ nanoplates in HT24h coating.

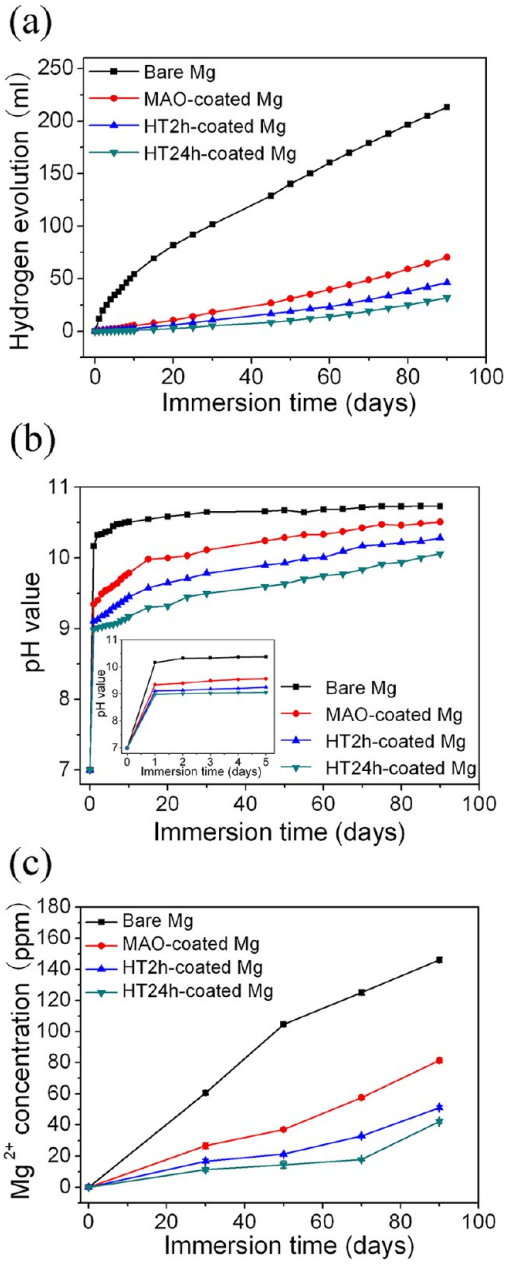

Figure 7. (a) Hydrogen volumes released by bare and coated Mg in PS solutions, (b) pH values, and (c) Mg^{2+} concentrations of the PS solutions immersing bare and coated Mg as a function of immersion time.

3.4. Evolution of Mechanical Integrity of Bare and Coated Mg in PS Solution. During the weeks following an operation, bone self-healing cannot provide sufficient strength;[6] therefore, bone fixation implants should provide long-term mechanical support for fractured bones. To evaluate the mechanical integrity of the bare and coated Mg after immersion in PS solution, three-point bending tests were performed using cylinder-like samples, and the changes in the maximum bending forces (BF_{max}) of the samples with immersion time is shown in Figure 8a. These values were derived from the curves of bending load versus displacement, as representatively presented in Figure 8b. Prior to immersion, the MAO, HT2h, and HT24h coated Mg exhibit BF_{max} values similar to that of bare Mg (approximately 1333 ± 37.3 N), suggesting that the addition of

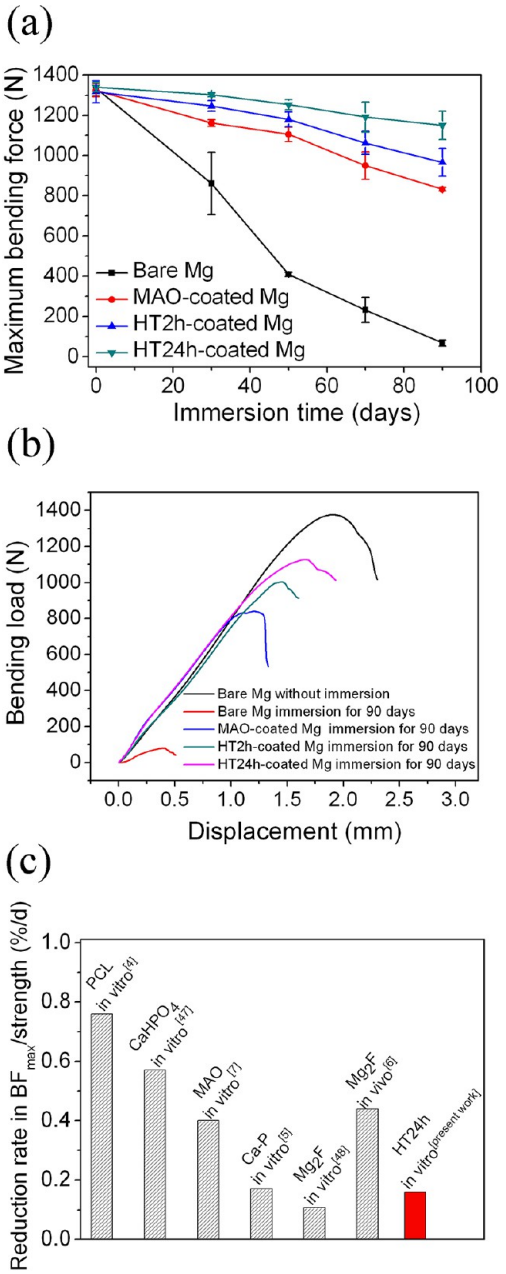

Figure 8. (a) Changes in maximum bending loads of bare and coated Mg with time of immersion in PS solution; (b) representative bending load versus displacement curves, in which the tested samples are marked; (c) in vitro/in vivo percentage reduction rate in BF_{max} or strength of literature-mentioned coatings coated Mg alloys and our HT24h coated Mg.

the coatings onto Mg had no obvious impact on its mechanical strength. Following immersion, not only bare Mg but also the coatings coated Mg display a decrease in BF_{max}. However, the decreased amplitudes of BF_{max} are quite different for the samples. After 90 days of immersion, for example, the bare Mg as well as MAO, HT2h, and HT24h coated Mg exhibit 94.9%, 37.2%, 26.6%, and 14.2% decrease in BF_{max}, respectively. The result indicates that HT24h coated Mg can sustain longer-term mechanical integrity. This is ascribed to the strong barrier to corrosive fluid provided by HT24h coating, resulting from the sealing of pores in the MgO with HA and $Mg(OH)_2$ in HT24h coating, so that the pitting corrosion of the underlying Mg presented in MAO and HT2h coatings was greatly inhibited in HT24h coating (Figures 2d, 3d, 4d, and 7c). As previously demonstrated, severe pitting corrosion of Mg and its alloys could lead to premature loss of their mechanical strength.[40]

A great deal of research has been conducted to investigate the mechanical integrity of Mg alloys augmented with a variety of coatings after immersion in vitro or implantation in vivo. For instance, PCL coated AZ91 alloy has been reported a 46% reduction in compressive strength after immersion in SBF for 60 days;[4] $CaHPO_4$ coated Mg alloy has been demonstrated a 32% decrease in compressive strength after 8 weeks of immersion in modified Hank's solution;[47] Imwinkelried et al. reported that BF_{max} of MAO coated WE43 alloy reduced 34% after immersion in SBF for 12 weeks and 8% after implantation in vivo for 12 weeks, respectively.[7] Noticeably, Yang et al. demonstrated that $CaHPO_4$–$Ca_3(PO_4)_2$ coated AZ31b alloy had a 15% decrease in BF_{max} after 90 days of immersion in SBF,[5] and MgF_2 coated AZ31b alloy exhibited a 13% decrease in BF_{max} after 120 days of immersion in SBF.[48] However, Thomann et al. reported that the reduction in BF_{max} of MgF_2 coated $MgCa_{0.8}$ alloy was about 40% after implantation in rabbits for 3 months.[6] It has been reported that MAO coated WE43 alloy is far less prone to a drop in BF_{max} in vivo than in vitro after the same duration.[7] Moreover, LAE442 alloy was observed to degrade much slower in vivo than in vitro.[49] Thus, somewhat perplexing is the fact that the reduction in the BF_{max} of MgF_2-coated alloys in vitro[48] is less than that of MgF_2-coated alloys in vivo.[6] For a convenient comparison of the protective efficacy of our HT24h coating with the aforementioned coatings, Figure 8c highlights their percentage reduction rate in strength or BF_{max} (e.g., the ratio of the percentage reduction in strength or BF_{max} and duration time). It is shown that our HT24h coated Mg exhibits the lowest in vitro percentage reduction rate in strength/BF_{max} compared to PCL,[4] $CaHPO_4$,[47] and MAO[7] coated Mg alloys, revealing much higher corrosion protective effect of the novel bilayer coating on the underlying Mg-based substrate.

3.5. Corrosion Resistance of Coated Mg As Identified by Electrochemical Tests. Figure 9a shows the potentiodynamic polarization curves of bare and coated Mg discs tested in PS solution, from which the corrosion potentials (E_{corr}) and corrosion current densities (i_{corr}) of the samples can be drawn as summarized in Table 1. HT24h and HT2h coated Mg reveal a significant decrease in i_{corr} compared to bare and MAO coated Mg. In particular, the i_{corr} of HT24h coated Mg is 4 orders of magnitude lower than that of bare Mg and two orders below that of MAO coated Mg. Meanwhile, HT2h and HT24h coated Mg are ennobled in E_{corr} compared to bare and MAO coated Mg. The lower i_{corr} and more positive E_{corr} imply higher corrosion resistance. The polarization results suggest that HT coatings (especially HT24h coating) can provide more effective protection for Mg substrates.

In order to further investigate protective efficacy of the coatings on Mg, EIS tests were also carried out. Figure 9b exhibits the Nyquist plots drawn from the EIS spectra of bare and the coated Mg discs in PS solution. The plots of MAO, HT2h, and HT24h coated Mg display a similar feature with two capacitance loops: the high frequency one is associated with corrosive solution penetrating into the coatings and the low frequency one is related to Faradaic charge transfer reaction at the interface of coating/substrate.[50−52] Different from the coated Mg, the bare Mg shows an inductive loop in its Nyquist plot at a low frequency due to the absorption of metastable

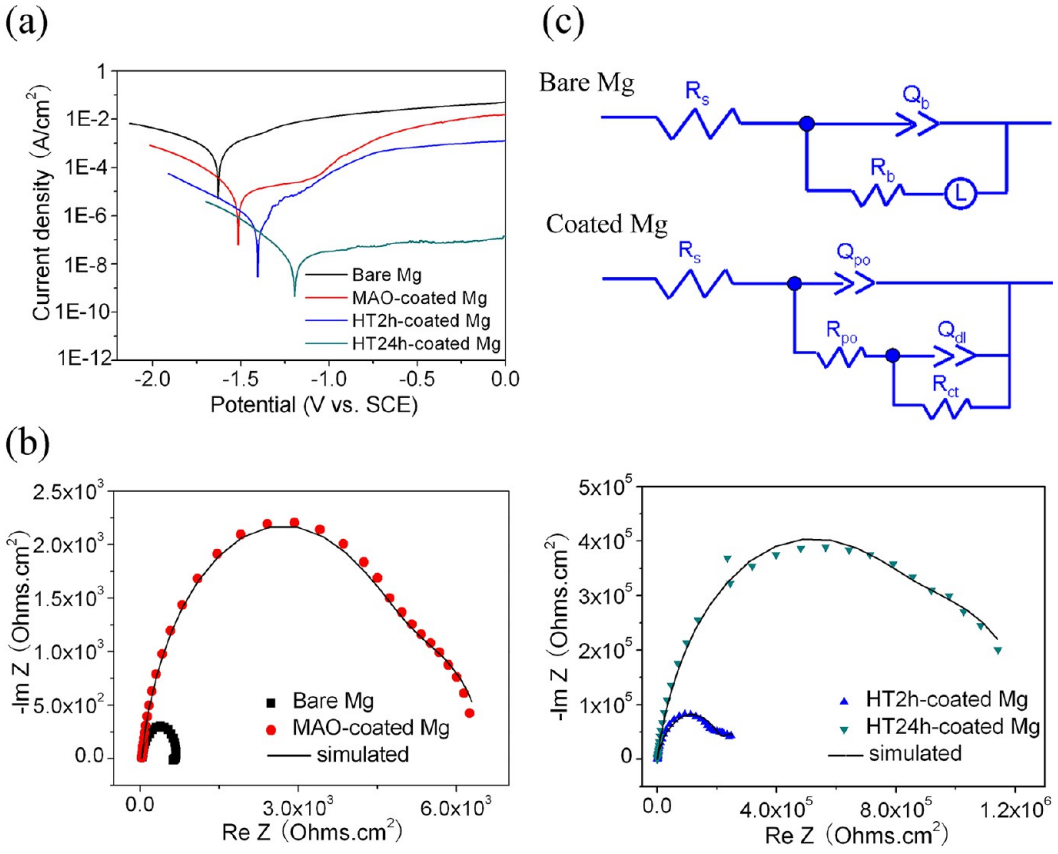

Figure 9. (a) Polarization curves and (b) Nyquist plots of EIS spectra of bare and coated Mg discs measured in PS solution, (c) equivalent circuits used to fit the impedance data of bare and coated Mg discs.

Table 1. Corrosion Potentials (E_{corr} Values) and Corrosion Current Densities (i_{corr} Values) Obtained from the Polarization Curves of Bare, MAO and HT coated Mg Discs and EIS Fitted Parameters of the Equivalent Circuits for Bare, MAO and HT Coated Mg Discs in PS Solution

samples	bare Mg	MAO coated Mg	HT2h coated Mg	HT24h coated Mg
E_{corr} (V vs SCE)	−1.63	−1.56	−1.40	−1.19
i_{corr} (A/cm^2)	7.62×10^{-4}	6.59×10^{-6}	5.50×10^{-7}	1.10×10^{-8}
R_s (Ω)	40.55	33.48	38.5	39
R_{po} (Ωcm^2)		5.22×10^3	2.71×10^5	1.00×10^6
Q_{po} (μF cm^{-2})		7.60	0.33	0.13
n_{po}		0.8768	0.7861	0.8537
R_b (Ωcm^2)	651.4			
Q_b (μF cm^{-2})	10.70			
n_b	0.896			
R_{ct} (Ωcm^2)		1.13×10^3	9.27×10^4	2.70×10^5
Q_{dl} (μF cm^{-2})		392.50	26.77	3.30
n_{dl}		0.8462	0.9084	0.953

intermediate Mg^+ and hydrogen release during Mg degradation, implying that the substrate has been corroded by the solution.[51,53] Based on the architecture of the coatings, equivalent circuits used to fit the impedance data of bare and coated Mg are shown in Figure 9c. In the figure, R_s is the resistance of the tested solution; R_b, L, and Q_b are the charge transfer resistance, inductor, and capacitance of electric double layer at the Mg/solution interface, respectively; Q_{dl} and R_{ct} represent the capacitance of electric double layer and charge transfer resistance at the coating/substrate interface; Q_{po} and R_{po} are the capacitance and solution penetration resistance of MAO, HT2h, and HT24h coatings. It is confirmed by Figure 9b that the fitted data derived from the equivalent circuits are in good agreement with experimental data, with deviation less than 5%.

The fitted parameters of the equivalent circuits are presented in Table 1. It can be seen that R_s values of the samples tested solutions are similar, due to the fixed compositions of the solutions and position between the working electrode and reference electrode during the tests. It is worth noticing that the R_{po} values of HT2h and HT24h coated Mg are about two and three orders greater than that of MAO coated Mg, respectively, suggesting that sealing the pores in MgO layer with HA and/or $Mg(OH)_2$ can effectively inhibit the penetration of corrosive solution into the coatings. Meanwhile, the R_{ct} values of HT24h coated Mg are nearly two orders greater than that of MAO

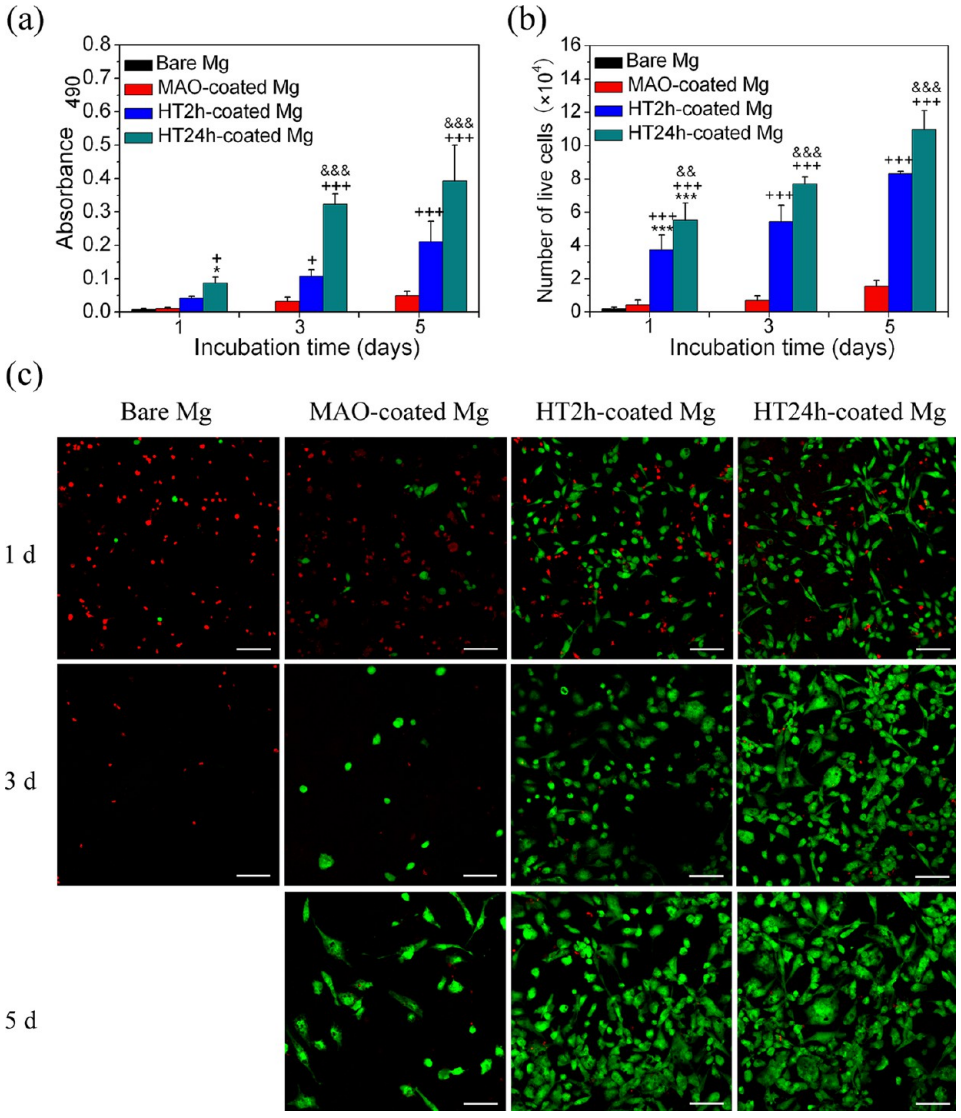

Figure 10. (a) MTT assay of osteoblasts incubated on bare and the coated Mg for 1, 3, and 5 days, (b) the number of live cells counted from (c) fluorescent images of osteoblasts cultured on bare and the coated Mg for 1, 3, and 5 days (scale bar: 100 μm). Data are presented as the mean ± SD, $n = 4$, (*) $p < 0.05$ compared with bare Mg, (+) $p < 0.05$, and (+++) $p < 0.001$ compared with MAO coated Mg, and (&&) $p < 0.01$ and (&&&) $p < 0.001$ compared with HT2h coated Mg.

coated Mg, providing further proof of the superior corrosion resistance of HT24h coating.

Since capacitor in EIS often does not behave ideally due to the complicated corrosion process at the tested sample/solution interface, the constant phase elements (CPEs) representing a shift from the ideal capacitor are used. The impedance of CPE is defined as[54]

$$Z_{CPE} = [Q(j\omega)^n]^{-1}$$

where Q is the capacitance value of the tested coating, $j\omega$ is the complex variable for sinusoidal perturbations with $w = 2\pi f$, and n is the exponent of CPE representing deviation from the ideal capacitance, the value of n ranges between 0 and 1. As shown in Table 1, the obtained values of n_{po} and n_{dl} reveal smaller deviation from 1, indicating smaller deviation of the coatings from ideal capacitances. On the other hand, the capacitance of Q can be expressed as follows:[52]

$$Q = \frac{\varepsilon_0 \varepsilon A}{L}$$

where ε_0 and ε are the dielectric constants of a vacuum and the tested coating, A and L are the surface area and the thickness of the tested coating, respectively. Considering that MAO and HT coatings have quite similar surface areas and thicknesses (Figure 1) and such short-term duration (15 min) of EIS testing could not significantly alter surface areas and thicknesses of the coatings, it can be thought that the values of Q depend only on the dielectric constants of the coatings. As listed in Table 1, the fitted Q_{po} values of the coatings follow the order: MAO > HT2h > HT24h, revealing that HT24h coating has a dielectric constant smaller than that of HT2h coating and far smaller than that of MAO coating. As known, the more porous and defective a coating is, the higher dielectric constant it has.[52,55] Thus, the far lower Q_{po} of HT24h coating is attributed to its far more compact structure compared with MAO coating, which is more beneficial to preventing the underneath Mg from corrosion. Meanwhile the lower Q_{dl} value of HT24h coated Mg compared to MAO and HT2h coated Mg also indicates a better anticorrosion performance of the former, as suggested elsewhere.[52]

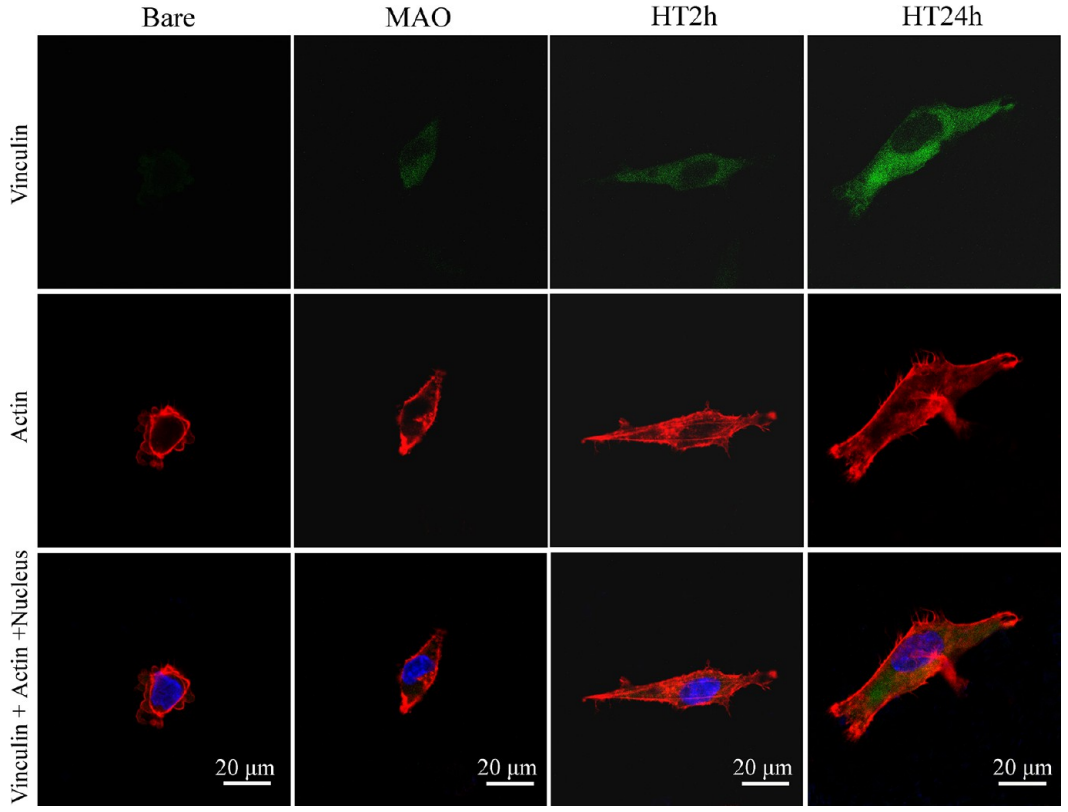

Figure 11. Vinculin (green), actin (red), and cell nucleus (blue) fluorescence images of osteoblasts after 24 h of culture on bare Mg as well as MAO, HT2h, and HT24h coated Mg.

3.6. Cytocompatibility of Coated Mg. MTT assay of osteoblasts on MAO, HT2h, and HT24h coated Mg was performed together with bare Mg after 1, 3, and 5 days of incubation, as shown in Figure 10a. It actually reflects mitochondrial activity (thus metabolic condition) of cells. At each time point, the mitochondrial activity of cells is very low on bare Mg and even cannot be detected on days 3 and 5; however, it significantly enhances on the coated Mg following the order: HT24h > HT2h > MAO. It is indicated that coating Mg with HT24h can greatly improve the viability of cells. Figure 10b shows the counting assay of live cells on bare and coated Mg, based on the fluorescent observations of stained cells as depicted in Figure 10c. Bare Mg has little live cells adhered, while pronounced live cells have been observed on the coated Mg. The coated Mg all show significant increase in the number of live cells with prolonging incubation time. At each time point, live cells are more in number on HT24h coated Mg compared to HT2h coated Mg, and much more pronounced compared to MAO coated Mg, indicating that HT24h coated Mg is more beneficial to adhesion and proliferation of cells than HT2h and MAO coated Mg.

The adhesion of cells to a material is achieved via the formation of focal adhesion (FA).[56] The characterization of FA and actin cytoskeleton would provide evidence on how a material affects cell adhesion.[57,58] As a marker to identify FA contacts, vinculin is a membrane bound protein involved in FA and acts as a linker between integrins and actin cytoskeleton.[59] Figure 11 shows vinculin−actin−nucleus tricolors staining fluorescence images of cells on bare and coated Mg after 1 day of culture. The vinculin denoted FA contacts cannot be observed in cells on bare Mg; however, they are visible a little in cells on MAO and HT2h coated Mg and more pronounced in cells on HT24h coated Mg. Noticeably, the FA contacts are distributed over the peripheral and central regions of cells on HT24h coated Mg, indicating that the cells bind well to HT24h coating. Furthermore, thicker and well organized filamentous actin bundles are observed in cells on HT24h and HT2h (especially HT24h) coated Mg compared to MAO coated Mg. The fluorescence images also show that the area of individual cell on HT24h coated Mg is significantly increased compared to that on the other coatings coated Mg, indicating a better spread of cells on the former.

As osteoblast is an arching-survival cell, the osteoblastic cytocompatibility of Mg alloys with and without coatings depends on two factors: the medium in which the cells are located and the surface features of a material to which the cells adhere (such as chemical composition and topography, etc.). For the medium environment, it has been reported that H_2-enriched DMEM (with a H_2 concentration of about 1.85%) can be well tolerated by preosteoblasts with more than 90% viability and the presence of such concentration of H_2 in the medium gives rise to a significantly higher ALP activity.[60] However, excessive H_2 release resulting from rapid degradation of Mg-based implants is a major concern,[61] the accumulation of subcutaneous H_2 gas can lead to cell damage and inhibit the healing process of fractured bone.[38] Regarding to the concentrations of released Mg^{2+}, Wong et al. found that cell viability in DMEM containing 50 ppm Mg^{2+} is significantly improved.[62] However, Mg^{2+} concentrations exceeding 150 ppm can have toxic effects on osteoblasts.[4] Moreover, a high Mg^{2+} concentration (200 ppm) can reduce the viability of preosteoblasts[62] and inhibit the proliferation of hMSC.[38] With respect to pH value, Shen et al. found that osteoblast viability was significantly enhanced with increasing pH up to

8−8.5.[63] It has to be pointed out that the alkalization caused by the corrosion of Mg can result in a fast increase in pH value of SBF to 10.5, which is undesirable for the adhesion, growth and proliferation of cells.[64,65] Noticeably, a recent study showed that coating Mg with $Mg(OH)_2$ was able to delay cell death; however, it resulted in reduced cell densities and abnormal cellular morphology compared to glass.[66] Our results concerning the mitochondrial activity, adhesion, and proliferation of osteoblasts have shown that cell viability is quite low on bare Mg, which can be attributed to a large amount of hydrogen evolution (Figure 7a), strong alkalization (to pH 10.17 at day 1 of immersion), and a high concentration of released Mg^{2+} (Figure 7c) as a result of the fast corrosion process. In contrast, MAO, HT2h, and HT24h coated Mg presented the enhanced mitochondrial activity, adhesion, and proliferation of osteoblasts, in which the best osteoblastic cytocompatibility was achieved with HT24h. This is related to the difference in corrosion protective effect of the coatings on Mg and consequent lightened extent of hydrogen evolution, alkalization, and release of Mg^{2+}. It could also depend on the surface chemical component and topography of the coatings. Previous studies have described the enhanced role of HA in promoting adhesion, proliferation and differentiation of cells, compared to polymers, MgO, and other inorganic components.[3,30,31] Our previous works have revealed that the topography of HA also plays a key role in the regulation of cell behavior. For example, Sr-HA nanorods with interrod spacing of less than 96 nm can enhance osteoblastic adhesion and proliferation compared to nanogranulated TiO_2 and Sr-HA.[32−34] Therefore, the architecture of an inner layer of pore-sealed MgO in conjunction with an outer layer of narrow interrod spaced HA nanorods endows HT24h coating with particularly good cytocompatibility.

4. CONCLUSIONS

A novel bilayer coating (HT24h) has been fabricated on Mg by hydrothermal treatment of microarc oxidized porous MgO layer containing Ca and P in an aqueous solution containing Ca-EDTA. The coating comprises an inner layer of MgO containing pores sealed with HA nanorods and $Mg(OH)_2$ nanoplates as well as an outer layer of narrow interrod spaced HA nanorods, in which the roots of the HA nanorods are embedded in the MgO matrix and the $Mg(OH)_2$ nanoplates are among the HA nanorods. We have determined that the migration of Ca^{2+} ions from the MgO layer plays a predominant role in HA nucleation, while Ca^{2+} ions supplied by the thermal dissociation of Ca-EDTA contribute to HA nucleation and play a predominant role in the growth of HA nanorods. Immersion tests of the porous MgO (termed as MAO), MgO containing $Mg(OH)_2$-sealing-pores (termed as HT2h) and HT24h coatings in PS solution indicate that cracking rather than delamination is a common feature in most areas of the coatings up to 90 days. Degradation is the cause of the thinning of the coatings, depending on the phase components of the coatings. MAO and HT2h coatings exhibit significant thinning owing to fast degradation of MgO; however, HT24h coating shows a quite small decrease in thickness, which can be attributed to the fact that the HA nanorods underwent quite slow degradation while the underlying MgO only underwent conversion to $Mg(OH)_2$ without dissolution of the $Mg(OH)_2$. Scratch tests reveal that after 90 days of immersion, HT24h coating retains relatively high bonding integrity, although the failure position under critical load changes from the interior of the MgO to a point between HA and MgO layers. However, MAO and HT2h coatings exhibit a relatively fast drop in bonding integrity, and the failure positions under critical loads change from the interiors of the MgO to the MgO/Mg interface for MAO coating or the upper $Mg(OH)_2$/MgO interface for HT2h coating. Compared to MAO and HT2h coatings, HT24h coating is shown to greatly reduce the degradation and thereby maintain sufficient mechanical integrity of Mg as well as enhance the mitochondrial activity, adhesion, and proliferation of osteoblasts.

■ ASSOCIATED CONTENT

Supporting Information

XRD patterns detected on the surface of MAO coating before and after HT for 2, 8, and 24 h as well as XPS spectrum and high-resolution spectra of P 2p and Ca 2p detected on the surface of MAO coating; TEM bright field images as well as EDX spectra, selected-area electron diffraction (SAED) patterns and high-resolution TEM (HRTEM) images taken from the nanoplate scratched from the surface of HT2h coating and nanorod scratched from the surface of HT24h coating; changes in P and Ca profiles on the cross-section of MgO layer before and after HT for 24 h and schematic diagram showing growth of $Mg(OH)_2$ nanoplates and HA nanorods on MgO layer during HT; SEM surface morphologies of the coating formed by MAO of pure Mg in an aqueous electrolyte containing 0.0135 M $Ca(OH)_2$, 0.02 M β-GP, and 0.125 M NaOH and subjected to HT in an aqueous solution containing 0.5 M NaOH at 90 °C for 24 h; SEM surface morphologies of the coating formed by MAO of pure Mg in an aqueous electrolyte containing 0.02 M β-GP and 0.125 M NaOH and subjected to HT in an aqueous solution containing 0.1 M Ca-EDTA and 0.5 M NaOH at 90 °C for 2, 8, and 24 h; cross-sectional views taken at the upper regions of the MAO coating immersed in PS solution for 30, 50, 70, and 90 days; cross-sectional views of MAO, HT2h, and HT24h coatings before and after immersion in PS solution for 30, 70, and 90 days, together with O and Mg profiles detected by EDX. This material is available free of charge via the Internet at http://pubs.acs.org.

■ AUTHOR INFORMATION

Corresponding Author

*Tel.: +86 02982665580. Fax: +86 02982663453. Email: yonghan@mail.xjtu.edu.cn.

Notes

The authors declare no competing financial interest.

■ ACKNOWLEDGMENTS

We appreciate the National Program on Key Basic Research Project (973 Program) of China (Grant number 2012CB619103) and National Natural Science Foundation of China (Grant No. 51371137, 51071120) for financially supporting this work.

■ REFERENCES

(1) Yun, Y. H. Revolutionizing Biodegradable Metal. *Mater. Today* **2009**, *12*, 22−32.

(2) Hermawan, H.; Dube, D.; Mantovani, D. Developments in Metallic Biodegradable Stents. *Acta Biomater.* **2009**, *6*, 1693−1697.

(3) Hornberger, H.; Virtanen, S.; Boccaccini, A. R. Biomedical Coatings on Magnesium Alloys − A Review. *Acta Biomater.* **2012**, *8*, 2442−2455.
(4) Wong, H. M.; Yeung, K. W.; Lam, K. O.; Tam, V.; Chu, P. K.; Luk, K. D.; Cheung, K. M. A Biodegradable Polymer-Based Coating to Control the Performance of Magnesium Alloy Orthopaedic Implants. *Biomaterials* **2010**, *31*, 2084−2096.
(5) Wang, Q.; Tan, L. L.; Xu, W. L.; Zhang, B. C.; Yang, K. Dynamic Behaviors of a Ca-P Coated AZ31B Magnesium Alloy during in Vitro and in Vivo Degradations. *Mater. Sci. Eng., B* **2011**, *176*, 1718−1726.
(6) Thomann, M.; Krause, C.; Angrisani, N.; Bormann, D.; Hassel, T.; Windhagen, H.; Meyer-Lindenberg, A. Angrisani. Influence of a Magnesium-Fluoride Coating of Magnesium-Based Implants (MgCa0.8) on Degradation in a Rabbit Model. *J. Biomed. Mater. Res., Part A* **2010**, *93*, 1609−1619.
(7) Imwinkelried, T.; Beck, S.; Iizuka, T.; Schaller, B. Effect of a Plasmaelectrolytic Coating on the Strength Retention of in Vivo and in Vitro Degraded Magnesium Implants. *Acta Biomater.* **2013**, *9*, 8643−8649.
(8) Li, L. C.; Gao, J. C.; Wang, Y. Evaluation of Cyto-Toxicity and Corrosion Behavior of Alkali-Heat-Treated Magnesium in Simulated Body Fluid. *Surf. Coat. Technol.* **2004**, *185*, 92−98.
(9) Gu, X. N.; Zheng, W.; Cheng, Y.; Zheng, Y. F. A Study on Alkaline Heat Treated Mg-Ca Alloy for the Control of the Biocorrosion Rate. *Acta Biomater.* **2009**, *5*, 2790−2799.
(10) Pereda, M. D.; Alonso, C.; Burgos-Asperilla, L.; del Valle, J. A.; Ruano, O. A.; Perez, P.; Fernandez Lorenzo de Mele, M. A. Corrosion Inhibition of Powder Metallurgy Mg by Fluoride Treatments. *Acta Biomater.* **2010**, *6*, 1772−1782.
(11) Chiu, K. Y.; Wong, M. H.; Cheng, F. T.; Man, H. C. Characterization and Corrosion Studies of Fluoride Conversion Coating on Degradable Mg Implants. *Surf. Coat. Technol.* **2007**, *202*, 590−598.
(12) Witte, F.; Fischer, J.; Nellesen, J.; Vogt, C.; Vogt, J.; Donath, T.; Beckmann, F. In Vivo Corrosion and Corrosion Protection of Magnesium Alloy LAE442. *Acta Biomater.* **2010**, *6*, 1792−1799.
(13) Wang, H. X.; Guan, S. K.; Wang, X.; Ren, C. X.; Wang, L. G. In Vitro Degradation and Mechanical Integrity of Mg-Zn-Ca Alloy Coated with Ca-Deficient Hydroxyapatite by the Pulse Electrodeposition Process. *Acta Biomater.* **2010**, *6*, 1743−1748.
(14) Song, Y.; Zhang, S.; Li, J.; Zhao, C.; Zhang, X. Electrodeposition of Ca-P Coatings on Biodegradable Mg Alloy: in Vitro Biomineralization Behavior. *Acta Biomater.* **2010**, *6*, 1736−1742.
(15) Chen, Y.; Song, Y.; Zhang, S.; Li, J.; Zhao, C.; Zhang, X. Interaction between a High Purity Magnesium Surface and PCL and PLA Coatings during Dynamic Degradation. *Biomed. Mater.* **2011**, *6*, 025005−025012.
(16) Gu, X. N.; Zheng, Y. F.; Lan, Q. X.; Cheng, Y.; Zhang, Z. X.; Xi, T. F.; Zhang, D. Y. Surface Modification of an Mg-1Ca Alloy to Slow Down Its Biocorrosion by Chitosan. *Biomed. Mater.* **2009**, *4*, 044109−044112.
(17) Xu, L.; Yamamoto, A. Characteristics and Cytocompatibility of Biodegradable Polymer Film on Magnesium by Spin Coating. *Colloids Surf., B* **2012**, *93*, 67−74.
(18) Zhang, X. P.; Zhao, Z. P.; Wu, F. M.; Wang, Y. L.; Wu, J. Corrosion and Wear Resistance of AZ91D Magnesium Alloy with and without Microarc Oxidation Coating in Hank's Solution. *J. Mater. Sci.* **2007**, *42*, 8523−8528.
(19) Yao, Z. P.; Li, L. L.; Jiang, Z. H. Adjustment of the Ratio of Ca/P in the Ceramic Coating on Mg Alloy by Plasma Electrolytic Oxidation. *Appl. Surf. Sci.* **2009**, *255*, 6724−6728.
(20) Gu, X. N.; Li, N.; Zhou, W. R.; Zheng, Y. F.; Zhao, X.; Cai, Q. Z.; Ruan, L. Q. Corrosion Resistance and Surface Biocompatibility of a Microarc Oxidation Coating on a Mg-Ca Alloy. *Acta Biomater.* **2011**, *7*, 1880−1889.
(21) Staiger, M. P.; Pietak, A. M.; Huadmai, J.; Dias, G. Magnesium and Its Alloys as Orthopedic Biomaterials: a Review. *Biomaterials* **2006**, *27*, 1728−1734.
(22) Zhang, J. F.; Zhang, W.; Yan, C. W.; Du, K. Q.; Wang, F. H. Corrosion Behaviors of Zn/Al-Mn Alloy Composite Coatings Deposited on Magnesium Alloy AZ31B (Mg-Al-Zn). *Electrochim. Acta* **2009**, *55*, 560−571.
(23) Han, Y.; Zhou, J.; Zhang, L.; Xu, K. A Multi-Scaled Hybrid Orthopedic Implant: Bone ECM-Shaped Sr-HA Nanofibers on the Microporous Walls of a Macroporous Titanium Scaffold. *Nanotechnology* **2011**, *22*, 275603−275614.
(24) Luo, H. H.; Cai, Q. H.; Wei, B. K.; Yu, B.; Li, D. J.; He, H.; Liu, Z. Effect of $(NaPO_3)_6$ Concentrations on Corrosion Resistance of Plasma Electrolytic Oxidation Coatings Formed on AZ91D Magnesium Alloy. *J. Alloys Compd.* **2008**, *464*, 537−543.
(25) Fischerauer, S. F.; Kraus, T.; Wu, X.; Tangl, S.; Sorantin, E.; Hanzi, A. C.; Loffler, J. F.; Uggowitzer, P. J.; Weinberg, A. M. In Vivo Degradation Performance of Micro-Arc-Oxidized Magnesium Implants: A Micro-CT Study in Rats. *Acta Biomater.* **2013**, *9*, 5411−5420.
(26) Lin, X.; Tan, L. L.; Zhang, Q.; Yang, K.; Hu, Z. Q.; Qiu, J. H.; Cai, Y. The in Vitro Degradation Process and Biocompatibility of a ZK60 Magnesium Alloy with a Forsterite-Containing Micro-arc Oxidation Coating. *Acta Biomater.* **2013**, *9*, 8631−8642.
(27) Duan, H. P.; Du, K. Q.; Yan, C. W.; Wang, F. H. Electrochemical Corrosion Behavior of Composite Coatings of Sealed MAO Film on Magnesium Alloy AZ91D. *Electrochim. Acta* **2006**, *51*, 2898−2908.
(28) Shang, W.; Chen, B. Z.; Shi, X. C.; Chen, Y.; Xiao, X. Electrochemical Corrosion Behavior of Composite MAO/Sol−Gel Coatings on Magnesium Alloy AZ91D using Combined Micro-arc Oxidation and Sol-Gel Technique. *J. Alloys Compd.* **2009**, *474*, 541−545.
(29) Jiang, Y. P.; Jia, T. H.; Gong, W. M.; Wooley, P. H.; Yang, S. Y. Titanium Particle-Challenged Osteoblasts Promote Osteoclastogenesis and Osteolysis in a Murine Model of Periprosthestic Osteolysis. *Acta Biomater.* **2013**, *9*, 7564−7572.
(30) Shadanbaz, S.; Dias, G. J. Calcium Phosphate Coatings on Magnesium Alloys for Biomedical Applications: A Review. *Acta Biomater.* **2012**, *8*, 20−30.
(31) Chen, S.; Guan, S. K.; Li, W.; Wang, H. X.; Chen, J.; Wang, Y. S.; Wang, H. T. In Vivo Degradation and Bone Response of a Composite Coating on Mg-Zn-Ca Alloy Prepared by Microarc Oxidation and Electrochemical Deposition. *J. Biomed. Mater. Res., Part B* **2012**, *100B*, 533−543.
(32) Han, Y.; Zhou, J. H.; Lu, S. M.; Zhang, L. Enhanced Osteoblast Functions of Narrow Interligand Spaced Sr-HA Nano-Fibers/Rods Grown on Microporous Titania Coatings. *Rsc Adv.* **2013**, *3*, 11169−11184.
(33) Zhou, J. H.; Li, B.; Lu, S. M.; Zhang, L.; Han, Y. Regulation of Osteoblast Proliferation and Differentiation by Interrod Spacing of Sr-HA Nanorods on Microporous Titania Coatings. *Acs Appl. Mater. Interfaces* **2013**, *5*, 5358−5365.
(34) Zhou, J. H.; Han, Y.; Lu, S. M. Direct Role of Interrod Spacing in Mediating Cell Adhesion on Sr-HA Nanorod-Patterned Coatings. *Int. J. Nanomed.* **2014**, *9*, 1243−1260.
(35) Tomozawa, M.; Hiromoto, S. Microstructure of Hydroxyapatite- and Octacalcium Phosphate-Coatings Formed on Magnesium by a Hydrothermal Treatment at Various pH Values. *Acta Mater.* **2011**, *59*, 355−363.
(36) Hiromoto, S.; Tomozawa, M. Hydroxyapatite Coating of AZ31 Magnesium Alloy by a Solution Treatment and Its Corrosion Behavior in NaCl Solution. *Surf. Coat. Technol.* **2011**, *205*, 4711−4719.
(37) Narayanan, T. S. N. S.; Park, I. S.; Lee, M. H. Strategies to Improve the Corrosion Resistance of Microarc Oxidation (MAO) Coated Magnesium Alloys for Degradable Implants: Prospects and Challenges. *Prog. Mater. Sci.* **2014**, *60*, 1−71.
(38) Chen, X. B.; Nisbet, D. R.; Li, R. W.; Smith, P. N.; Abbott, T. B.; Easton, M. A.; Zhang, D. H.; Birbilis, N. Controlling Initial Biodegradation of Magnesium by a Biocompatible Strontium Phosphate Conversion Coating. *Acta Biomater.* **2014**, *10*, 1463−1474.
(39) Liang, J.; Srinivasan, P. B.; Blawert, C.; Stormer, M.; Dietzel, W. Electrochemical Corrosion Behavior of Plasma Electrolytic Oxidation

Coatings on AM50 Magnesium Alloy Formed in Silicate and Phosphate Based Electrolytes. *Electrochim. Acta* **2009**, *54*, 3842−3850.
(40) Lin, X.; Yang, X. M.; Tan, L. L.; Li, M.; Wang, X.; Zhang, Y.; Yang, K.; Hu, Z. Q.; Qiu, J. H. In Vitro Degradation and Biocompatibility of a Strontium-Containing Micro-arc Oxidation Coating on the Biodegradable ZK60 Magnesium Alloy. *Appl. Surf. Sci.* **2014**, *288*, 718−726.
(41) Wang, J.; He, Y. H.; Maitz, M. F.; Collins, B.; Xiong, K. Q.; Guo, L. S.; Yun, Y. H.; Wan, G. J.; Huang, N. A Surface-Eroding Poly (1, 3-Trimethylene Carbonate) Coating for Fully Biodegradable Magnesium-Based Stent Applications: Toward Better Biofunction, Biodegradation and Biocompatibility. *Acta Biomater.* **2013**, *9*, 8678−8689.
(42) Abdal-Hay, A.; Dewidar, M.; Lim, J. K. Biocorrosion Behavior and Cell Viability of Adhesive Polymer Coated Magnesium Based Alloys for Medical Implants. *Appl. Surf. Sci.* **2012**, *261*, 536−546.
(43) ASTM. *Standard Practice for Laboratory Immersion Corrosion Testing of Metals*; ASTM-G31−72; American Society for Testing and Materials: Philadelphia, PA, 2004.
(44) Filgueiras, M. R. T.; Mkhonto, D.; de Leeuw, N. H. Computer Simulations of the Adsorption of Citric Acid at Hydroxyapatite Surfaces. *J. Cryst. Growth* **2006**, *294*, 60−68.
(45) De Leeuw, N. H. Computer Simulations of Structures and Properties of the Biomaterial Hydroxyapatite. *J. Mater. Chem.* **2010**, *20*, 5376−5389.
(46) Xia, S. J.; Yue, R.; Rateick, R. G.; Birss, V. I. Electrochemical Studies of AC/DC Anodized Mg Alloy in NaCl Solution. *J. Electrochem. Soc.* **2004**, *151*, B179−B187.
(47) Liao, Y.; Chen, D. S.; Niu, J. L.; Zhang, J.; Wang, Y. P.; Zhu, Z. J.; Yuan, G. Y.; He, Y. H.; Jiang, Y. In Vitro Degradation and Mechanical Properties of Polyporous $CaHPO_4$-Coated Mg-Nd-Zn-Zr Alloy as Potential Tissue Engineering Scaffold. *Mater. Lett.* **2013**, *100*, 306−308.
(48) Yan, T. T.; Tan, L. L.; Xiong, D. S.; Liu, X. J.; Zhang, B. C.; Yang, K. Fluoride Treatment and in Vitro Corrosion Behavior of an AZ31B Magnesium Alloy. *Mater. Sci. Eng., C* **2010**, *30*, 740−748.
(49) Witte, F.; Fischer, J.; Nellesen, J.; Crostack, H. A.; Kaese, V.; Pisch, A.; Beckmann, F.; Windhagen, H. In Vitro and in Vivo Corrosion Measurements of Magnesium Alloys. *Biomaterials* **2006**, *27*, 1013−1018.
(50) Song, D.; Ma, A. B.; Jiang, J. H.; Lin, P. H.; Yang, D. H.; Fan, J. F. Corrosion Behavior of Bulk Ultra-Fine Grained AZ91D Magnesium Alloy Fabricated by Equal-Channel Angular Pressing. *Corros. Sci.* **2011**, *53*, 362−373.
(51) Song, G.; Atrens, A.; St John, D.; Wu, X.; Nairn, J. The Anodic Dissolution of Magnesium in Chloride and Sulphate Solutions. *Corros. Sci.* **1997**, *39*, 1981−2004.
(52) Zhang, Y. J.; Yan, C. W.; Wang, F. H.; Li, W. F. Electrochemical Behavior of Anodized Mg Alloy AZ91D in Chloride Containing Aqueous Solution. *Corros. Sci.* **2005**, *47*, 2816−2831.
(53) Baril, G.; Pebere, N. The Corrosion of Pure Magnesium in Aerated and Deaerated Sodium Sulphate Solutions. *Corros. Sci.* **2001**, *43*, 471−484.
(54) Fekry, A. M.; Ameer, M. A. Electrochemistry and Impedance Studies on Titanium and Magnesium Alloys in Ringer's Solution. *Int. J. Electrochem. Sci.* **2011**, *6*, 1342−1354.
(55) Xin, Y.; Jiang, J.; Huo, K.; Tang, G.; Tian, X.; Chu, P. K. Corrosion Resistance and Cytocompatibility of Biodegradable Surgical Magnesium Alloy Coated with Hydrogenated Amorphous Silicon. *J. Biomed. Mater. Res., Part A* **2009**, *89*, 717−726.
(56) Geiger, B.; Spatz, J. P.; Bershadsky, A. D. Environmental Sensing through Focal Adhesions. *Nat. Rev. Mol. Cell. Biol.* **2009**, *10*, 21−33.
(57) Lim, J. Y.; Dreiss, A. D.; Zhou, Z. Y.; Hansen, J. C.; Siedlecki, C. A.; Hengstebeck, R. W.; Cheng, J.; Winograd, N.; Donahue, H. J. The Regulation of Integrin-Mediated Osteoblast Focal Adhesion and Focal Adhesion Kinase Expression by Nanoscale Topography. *Biomaterials* **2007**, *28*, 1787−1797.
(58) Seo, C. H.; Jeong, H.; Furukawa, K. S.; Suzuki, Y.; Ushida, T. The Switching of Focal Adhesion Maturation Sites and Actin Filament Activation for MSCs by Topography of Well-Defined Micropatterned Surfaces. *Biomaterials* **2013**, *34*, 1764−1771.
(59) Matschegewski, C.; Staehlke, S.; Loeffler, R.; Lange, R.; Chai, F.; Kern, D. P.; Beck, U.; Nebe, B. J. Cell Architecture-Cell Function Dependencies on Titanium Arrays with Regular Geometry. *Biomaterials* **2010**, *31*, 5729−5740.
(60) Wong, H. M.; Zhao, Y.; Tam, V.; Wu, S. L.; Chu, P. K.; Zheng, Y. F.; To, M. K. T.; Leung, F. K. L.; Luk, K. D. K.; Cheung, K. M. C.; Yeung, K. W. K. In Vivo Stimulation of Bone Formation by Aluminum and Oxygen Plasma Surface-Modified Magnesium Implants. *Biomaterials* **2013**, *34*, 9863−9876.
(61) Zberg, B.; Uggowitzer, P. J.; Löffler, J. F. MgZnCa Glasses without Clinically Observable Hydrogen Evolution for Biodegradable Implants. *Nat. Mater.* **2009**, *8*, 887−891.
(62) Wong, H. M.; Wu, S. L.; Chu, P. K.; Cheng, S. H.; Luk, K. D. K.; Cheung, K. M. C.; Yeung, K. W. K. Low-Modulus Mg/PCL Hybrid Bone Substitute for Osteoporotic Fracture Fixation. *Biomaterials* **2013**, *34*, 7016−7032.
(63) Shen, Y. H.; Liu, W. C.; Wen, C. Y.; Pan, H. B.; Wang, T.; Darvell, B. W.; Lu, W. W.; Huang, W. H. Bone Regeneration: Importance of Local pH Strontium-Doped Borosilicate Scaffold. *J. Mater. Chem.* **2012**, *22*, 8662−8670.
(64) Song, G. L.; Song, S. Z. A Possible Biodegradable Magnesium Implant Material. *Adv. Eng. Mater.* **2007**, *9*, 298−302.
(65) Xu, L. P.; Pan, F.; Yu, G. N.; Yang, L.; Zhang, E. L.; Yang, K. In Vitro and In Vivo Evaluation of the Surface Bioactivity of a Calcium Phosphate Coated Magnesium Alloy. *Biomaterials* **2009**, *30*, 1512−1523.
(66) Lorenz, C.; Brunner, J. G.; Kollmannsberger, P.; Jaafar, L.; Fabry, B.; Virtanen, S. Effect of Surface Pre-Treatments on Biocompatibility of Magnesium. *Acta Biomater.* **2009**, *5*, 2783−2789.